Computational Materials Science 207 (2022) 111283

Contents lists available at ScienceDirect

Computational Materials Science

journal homepage: www.elsevier.com/locate/commatsci

Effects of interatomic potential on fracture behaviour in single- and bicrystalline tungsten

Praveenkumar Hiremath [a,*], Solveig Melin [a], Erik Bitzek [b,c], Pär A.T. Olsson [a,d]

[a] Division of Mechanics, Lund University, Box 118, Lund, SE-221 00, Sweden
[b] Friedrich-Alexander-Universität Erlangen-Nürnberg, Department for Materials Science and Engineering, Institute I, 91058 Erlangen, Germany
[c] Computational Materials Design, Max–Planck-Institut für Eisenforschung GmbH, 40237 Düsseldorf, Germany
[d] Materials Science and Applied Mathematics, Malmö University, SE-205 06 Malmö, Sweden

ARTICLE INFO

Keywords:
Tungsten
Molecular statics
Fracture mechanisms
Grain-boundary cohesion
Critical stress intensity factor
Density functional theory

ABSTRACT

In the present work, we have evaluated the performance of different embedded atom method (EAM) and second-nearest neighbour modified embedded atom method (2NN-MEAM) potentials based on their predictive capabilities for modelling fracture in single- and bicrystalline tungsten. As part of the study, a new 2NN-MEAM was fitted with emphasis on reproducing surface, unstable stacking fault and twinning energies as derived from density functional theory (DFT) modelling. The investigation showed a systematic underestimation of surface energies by most EAM potentials, and a significant variation in unstable stacking and twinning fault energies. Moreover, the EAM potentials in general lack the ability to reproduce the DFT traction–separation (TS) curves. The shorter interaction length and higher peak stress of the EAM TS curves compared to the 2NN-MEAM and DFT TS curves result in one order of magnitude higher lattice trapping than for cracks studied with 2NN-MEAM. These differences in lattice trapping can lead to significant qualitative differences in the fracture behaviour. Overall, the new 2NN-MEAM potential best reproduced fracture-relevant material properties and its results were consistent with fracture experiments. Finally, the results of fracture simulations were compared with analytical predictions based on Griffith and Rice theories, for which emerging discrepancies were discussed.

1. Introduction

Refractory metals have long been considered for plasma-facing components (PFC) in nuclear fusion reactors. In particular, tungsten (W) and its alloys have emerged as the most promising candidate material for PFC [1,2] in light of their high melting temperature, high temperature strength, high thermal conductivity, low thermal expansion coefficient and high sputtering resistance [3–10]. However, tungsten exhibits limited ductility at low temperature and becomes ductile only above the brittle to ductile transition temperature (BDTT), which is in the approximate range of 100–200 °C [11,12] and 150–500 °C [12–19] for single- and polycrystalline forms, respectively, resulting in limitations on its applications. Like in other body-centred cubic (BCC) metals, the brittle-to-ductile transition (BDT) results from the competition between two mechanisms that dissipate elastic strain energy: bond breaking at low temperatures and thermally activated dislocation slip at elevated temperatures [20–22]. Materials that show such BDT are therefore often referred to as semi-brittle.

Atomistic simulations are ideally positioned to study the crack-tip processes underlying the BDT [23]. The reliability of such simulations depends on a wide range of factors, including applied boundary conditions, sample size, and in case of dynamic simulations, also the applied strain rate. But more profoundly, it depends critically on the used interatomic potential's capability to accurately reproduce the underlying mechanisms and their relative importance at a given strain rate and temperature. Semi-empirical many-body potentials, like the ones based on the embedded atom method (EAM) or modified embedded atom method (MEAM) that are often used for BCC metals, were traditionally fitted to relatively small databases, typically including lattice parameter, elastic constants, cohesive energy and vacancy formation energy [24–27]. More recently, potentials are fitted to large databases of structures and forces obtained by density functional theory (DFT) calculations [28]. Such procedures have enabled the incorporation of fracture-relevant properties in the fitting, such as generalized stacking faults and free surface energy. In both cases, however, the choice of properties and the weights given to different structures during the fitting process lead to potentials that are optimized for certain applications or areas of study. This results in a lack of transferability, i.e., a reduced ability to correctly model structures or calculate properties

---

* Corresponding author.
E-mail address: praveenkumar.hiremath@mek.lth.se (P. Hiremath).

https://doi.org/10.1016/j.commatsci.2022.111283
Received 18 November 2021; Received in revised form 11 February 2022; Accepted 13 February 2022
Available online 4 March 2022

that were not included in the fit. Recently, the transferability problem is being addressed through the development of machine learning potentials [29]. However, these are currently still too computationally intensive to perform the large-scale atomistic simulations necessary to study complex crack-tip processes in 3D [30]. Even though tungsten – thanks to its elastic isotropy – is widely used as model material to study fracture in BCC metals, currently no W potentials exist that have been developed with the focus on fracture simulations. Most available W potentials are designed for either radiation-induced damage modelling or are "general purpose" potentials, with generally limited predictability in terms for crack-tip relevant properties, see e.g. [31,32]. It is therefore crucial to assess the applicability of existing W potentials to study fracture. Such a systematic study is the focus of the present paper. In addition, we present a MEAM potential that was specifically generated for the purpose of modelling cracks in W.

Furthermore, continuum models of polycrystalline material failure require information regarding grain boundary (GB) fracture behaviour since they often serve as preferred fracture paths [33–37]. But, there is a lack of reliable experimental and atomistic studies of such interfaces. Therefore, we expand the scope of the paper beyond single-crystals and also evaluate the potentials for fracture behaviour of selected GBs. The specific objectives of the present work are summarized as:

- Evaluate the applicability of the different potentials for fracture studies.
- Systematically investigate the crack-tip response for single-crystals and GBs, and delineate the intrinsic potential features that govern the outcome.
- Assess the ability of existing theoretical frameworks to predict brittle and ductile crack-tip behaviour.

The paper is organized as follows: First, we provide a short overview of the fracture behaviour in tungsten single- and bicrystals. This is followed by a brief account of the theoretical fracture mechanics concepts required for this study. Then the simulation methodology is introduced along with the various EAM and MEAM potentials considered in the present work. In the results section, relevant potential properties are compared with DFT results, and the results of fracture simulations of single- and bicrystals are presented. In the discussion section, we compare the results with predictions from analytical theories and delineate the impact of inherent potential features on the fracture behaviour. Moreover, we assess the applicability of potentials for fracture simulations. Finally, we summarize the findings and present the conclusions.

2. Fracture behaviour of tungsten

2.1. Single-crystal fracture

Below the BDTT, single-crystalline fracture occurs in a brittle fashion along preferred crystallographic planes, namely the primary $\{100\}$ and secondary $\{110\}$ cleavage planes [11,12,38–50]. Cleavage fracture on these planes was shown to be anisotropic with respect to the cleavage direction [11,38–41,43,45,46]. Throughout this paper, crack systems are specified by the crack plane (klm) and the crack front $[uvw]$ direction, i.e., $(klm)[uvw]$.

The $\{100\}\langle 010\rangle$ crack system has been widely studied [12,39–46, 48–50]. At temperatures below the BDTT, and in particular at 77 K, the crack propagates on the $\{100\}$ plane, but river lines indicate that locally the crack propagation direction deviates from the macroscopic $\langle 001\rangle$ propagation direction [38,45], and local propagation along $\langle 110\rangle$ directions was observed [39,43,48].

Cracks on $\{100\}\langle 011\rangle$ have also been studied relatively frequently [11,38,43,45,46]. Also in this system, the crack remains on the initial $\{100\}$ cleavage plane. In contrast to cracks with $\langle 010\rangle$ crack front orientation, the river lines follow the macroscopic $\langle 01\bar{1}\rangle$ propagation direction.

Cracks initially situated on $\{011\}$ planes at low temperature also fracture in a brittle manner [38,40,43,45,46]. However, $\{011\}\langle 0\bar{1}1\rangle$ and $\{011\}\langle 100\rangle$ cracks both showed $\{100\}$ facets on the fracture surfaces [38,46], indicating a strong preference for local crack propagation on the primary cleavage plane. River lines were observed on the entire macroscopic $\{011\}$ fracture surface [38,46]. For $\{011\}\langle 0\bar{1}1\rangle$ cracks they follow the macroscopic crack propagation direction. In contrast, for $\{011\}\langle 100\rangle$ cracks, river lines perpendicular to the macroscopic crack propagation direction were observed [46].

While at 77 K brittle fracture was observed for both cracks oriented on $\{100\}$ and $\{011\}$ planes, a strong dependence of the fracture toughness on the crack front direction was observed. Cracks with $\langle 011\rangle$ fronts on these planes generally propagate easier than cracks with $\langle 010\rangle$ fronts, with fracture toughness values of K_{IC} around 2.8 and 3.8 MPa $\mathrm{m}^{1/2}$, respectively [11,38,46].

Only few studies exist for pre-cracks on higher-indexed fracture planes [46]. At 77 K, cracks initially on $\{111\}$ and $\{211\}$ showed brittle fracture [46]. Cracks with $\{111\}\langle 0\bar{1}1\rangle$ orientation displayed a strongly faceted surface, but the crystallographic orientation of these facets could not be identified [46]. In general, cracks initially on $\{211\}$ planes did not cleave on that plane, and their behaviour was strongly dependent on the crack front orientation. For instance, $\{211\}\langle 110\rangle$ cracks deviated onto $\{100\}$ planes, at which they formed large facets [46], while those on $\{211\}\langle 111\rangle$ propagated macroscopically on the initial $\{211\}$ plane, but with a rough fracture surface with many small facets — including $\{110\}$ facets [46].

Several computational studies have addressed the fracture behaviour of single-crystalline tungsten by atomistic simulations [20,33,38,51–58]. Although DFT is commonly used to delineate the traction–separation properties or assess the ideal brittle fracture toughness according to the Griffith theory [59], see e.g. [5,57,60–63], such calculations do not represent fracture simulations, as no crack is present. To the best of our knowledge, no DFT investigations of the crack-tip behaviour in W have been published so far. Neither are there any available fracture studies with numerical or analytical bond-order potentials or machine-learning potentials. Instead all simulations of cracks in W published so far rely on semi-empirical many-body potentials.

Quasi-static simulations of pre-existing atomically sharp cracks allow to determine the crack-tip events and to quantify the associated critical stress intensity factor and lattice trapping range [20,33,52]. Such simulations of cracks along $\{100\}\langle 010\rangle$ showed that, depending on the utilized potential and setup, either cleavage along the original $\{100\}$ plane [54,64] or propagation of the crack on the inclined $\{110\}$ planes can occur [51,64]. In contrast, cracks on $\{100\}\langle 011\rangle$ in simulations generally cleave on the initial $\{100\}$ plane [33,51,52,57, 64].

Cracks on $\{011\}$ planes were usually observed to cleave on the same plane, independent of the crack front orientation [51,54,57,64], although partial dislocation emission on the $\{111\}$ plane [52] as well as crack propagation on $\{121\}$ [53] were observed for a $\langle 0\bar{1}1\rangle$ crack front. No crack propagation on $\{100\}$ planes, which could explain the experimentally observed facet formation, was detected.

For cracks on the primary and secondary cleavage planes, in atomistic simulations, the lowest fracture toughness is usually reported for brittle fracture for $\{011\}\langle 0\bar{1}1\rangle$ cracks, followed by cracks on $\{100\}\langle 011\rangle$ [38]. However, for different potentials this order was found be reversed [64], which is in line with the experimental observation [38] that the difference in fracture toughness between the two systems is indeed very small. The preference in experiments of the higher energy $\{100\}$ fracture plane compared to the $\{011\}$ plane is believed to be due to the availability of four orthogonal easy propagation directions on the $\{100\}$ crack plane compared to only one easy propagation direction on the $\{110\}$ plane [38]. However, such behaviour cannot be captured by static atomistic modelling setups that only allow for short crack fronts with periodic boundary conditions [51].

The reason for the more difficult crack propagation along ⟨010⟩ than ⟨011⟩ directions is believed to lie in the larger lattice trapping associated with the latter crack front compared to the former [38]. Atomistic simulations based on EAM potentials have consistently shown this to be true for cracks on {100} and {011} planes [52,64].

Fracture along higher indexed planes has been studied in [33,51, 52,64]. For $\{111\}\langle 0\bar{1}1\rangle$ cracks, partial dislocation emission [52] and twinning [33] have been observed. In contrast, for $\{111\}\langle 11\bar{2}\rangle$ cracks the emission of full edge dislocations [33] as well as the emission of two partial dislocations up and down has been reported [52]. For $\{112\}\langle 11\bar{1}\rangle$ brittle fracture has been reported [33], but cracks on {113}, {114} and {115} crack planes generally showed crack-tip plasticity [33, 52].

2.2. Grain boundary fracture

Tungsten is a convenient model material to study GB fracture as – due its isotropic elasticity – the stress intensity factor for interface fracture does not become a complex number [65]. However, so far no experiments testing the toughness of individual GBs in tungsten have been published as such experiments are difficult to perform. In contrast, multiple studies have determined the fracture toughness of polycrystalline W and analysed its fracture behaviour, see e.g. [12, 15,66–77]. However, such studies cannot provide direct information on the toughness of individual GBs or GBs in general, as additional geometric effects influence whether inter- or transgranular fracture is observed [78].

Individual GBs in tungsten were tested by Liu and Shen [77,79]. In one study, they performed four-point bending tests on notched specimens containing ⟨100⟩ twist GBs. But because the notch was not directly situated on the GB, the fracture toughness of the GBs could not be directly determined [79].

Four-point bending tests for molybdenum bicrystals containing ⟨110⟩ symmetric tilt GBs, but without a notch, were used in the group of Yoshinaga [80,81]. They observed a correlation between fracture strength and relative GB energy, with small angle GBs as well as $\Sigma 3,\{112\}$, $\Sigma 3,\{111\}$ and $\Sigma 17b,\{334\}$ having much higher fracture strength than the other studied GBs [81].

Mikhailovskij et al. [82,83] used an original approach to estimate the strength of individual GBs in a polycrystal by controlled field evaporation in a field ion microscopy. Because the results were obtained under hydrostatic stress loading conditions, they are, however, not relevant to the study of mode I fracture.

Grain boundary fracture in tungsten was studied in detail using atomistic simulations by Möller and Bitzek [33]. Using an EAM potential, they highlighted the role of bond trapping – the generalization of lattice trapping to the bonding situation at interfaces – on the fracture toughness and crack-tip plasticity. In particular, they speculated that certain GBs could exhibit local fracture toughness values that are higher than the fracture toughness of single-crystals, even when they were oriented for fracture along the same plane [33]. Such effects are not captured by the often used proxy for toughness: the work of separation. This quantity can, however, be easily obtained from DFT calculations, see, e.g., [62,84]. For tungsten, such calculations have predicted the $\Sigma 3,(112)[1\bar{1}0]$ twin boundary to be the strongest of the studied tilt GBs [62].

3. Theoretical background

The following sections provide a short overview of the underlying theory of perfectly brittle fracture by Griffith [85] and the often-used criterion for crack-tip plasticity by Rice [21,86].

3.1. Brittle fracture

Within the Griffith model [85], the theoretical critical stress intensity factor K_{IG} under mode I loading for cleavage of a perfectly brittle material under plane strain conditions is given by [87]

$$K_{IG} = \sqrt{\frac{G_I}{B}}, \tag{1}$$

where G_I is the energy release rate due to the formation of two new surfaces, B is the appropriate crystal orientation dependent compliance constant [87,88]. For anisotropic cubic crystals under plane strain conditions, B can be expressed as

$$B = \sqrt{\frac{b_{11}b_{22}}{2}\left(\sqrt{\frac{b_{22}}{b_{11}}} + \frac{2b_{12}+b_{66}}{2b_{11}}\right)}. \tag{2}$$

The plane strain moduli b_{ij} can further be expressed in terms of elastic compliance constants s_{ij} along the orientation of interest as [87–89]

$$b_{11} = \frac{s_{11}s_{33} - s_{13}^2}{s_{33}},\ b_{22} = \frac{s_{22}s_{33} - s_{23}^2}{s_{33}}, \tag{3}$$

$$b_{12} = \frac{s_{12}s_{33} - s_{13}s_{23}}{s_{33}},\ b_{66} = \frac{s_{66}s_{33} - s_{26}^2}{s_{33}}. \tag{4}$$

For ideally brittle single-crystals, the energy release rate G_I in Eq. (1) is equivalent to ideal work of separation and takes the form $G_I = 2\gamma_s$, where $2\gamma_s$ is the total surface energy of the two newly created surfaces. For ideally brittle grain boundary fracture, G_I^{GB} can be expressed as [78,90]

$$G_I^{GB} = \gamma_s^1 + \gamma_s^2 - \gamma_{GB} \tag{5}$$

where γ_s^1, γ_s^2 and γ_{GB} are the surface energies of the adjoining grains 1 and 2 and the GB, respectively.

The Griffith theory is based on thermodynamics and continuum theory. The discreteness of the crystal lattice manifests itself in the so-called lattice trapping [20,22,38,52,91–93], as the surface cannot increase continuously but only by the breaking of discrete atomic bonds. This causes an atomically sharp crack to remain stable during loading until an upper limiting value K_+, higher than Griffith's stress intensity factor K_{IG} is reached. Likewise during unloading, the crack position remains unchanged until $K_- < K_{IG}$ is reached. The lattice trapping range, ΔK, is then defined as [22,91]

$$\Delta K = \frac{K_+}{K_-} - 1. \tag{6}$$

The analogue of lattice trapping for interfaces is commonly referred to as bond trapping, which includes the breaking of bonds in the structural units of GBs [22].

3.2. Crack-tip plasticity

According to Rice's theory [21,86], the analytical stress intensity factor necessary for dislocation emission, K_{IE}, is given by

$$K_{IE} = \sqrt{\frac{G_{IE}}{B}}, \tag{7}$$

where $G_{IE} = 8\frac{1+(1-\nu_{yx})\tan^2\phi}{(1+\cos\theta)\sin^2\theta}\gamma_{us}$ with γ_{us} and ν_{yx} corresponding to the unstable stacking fault energy and Poisson's ratio, respectively, and the angles, θ and ϕ, as defined in Fig. 1 [21,86]. We note that Eq. (7) is derived to predict dislocation emission exclusively, and therefore it does not account for concomitant crack-tip plasticity and cleavage processes. However, for the special case of GBs – depending on the crack-tip position – alternating dislocation emission and cleavage processes can be observed in quasi-static simulations. For such instances, Farkas [94] suggested that Eq. (7) serves as an upper limit estimate of the energy release rate.

Table 1
Herein considered EAM and MEAM potentials and the properties making up their fitting databases. TW indicates This Work and 'X's indicate if a potential was fitted to the specific property. The parameters, a_0, E_{coh}, C_{ij}, E_{vac}, and E_{SIA} correspond to the lattice parameter, cohesive energy, elastic constants, vacancy and self-interstitial energies, respectively. The data $\Delta E_{BCC\rightarrow FCC}$ and $\Delta E_{FCC\rightarrow HCP}$ represent the structural energy difference between phases, while "Liq. configs." indicate whether energies and/or forces attained from random configurations were utilized. The surface and unstable stacking fault energy are represented by γ_s and γ_{us}, respectively, while the equation of state for different phases is designated EOS.

Property	Potentials								
	EAM-1 [97,98]	EAM-2 [99]	EAM-3 [100]	EAM-4 [28]	EAM-5 [101]	EAM-6 [102]	EAM-7 [28]	MEAM-1 [54,103]	MEAM-2 TW
a_0	X	X	X	X	X	X	X	X	X
E_{coh}	X	X	X	X	X	X	X	X	X
C_{ij}	X	X	X	X	X	X	X	X	X
E_{vac}		X	X	X	X	X	X	X	
E_{SIA}	X	X	X	X	X		X		
$\Delta E_{BCC\rightarrow FCC}$		X		X			X	X	X
$\Delta E_{FCC\rightarrow HCP}$								X	X
Liq. configs.				X			X		
γ_s								X	X
γ_{us}									X
BCC EOS								X	X
FCC/HCP EOS									X

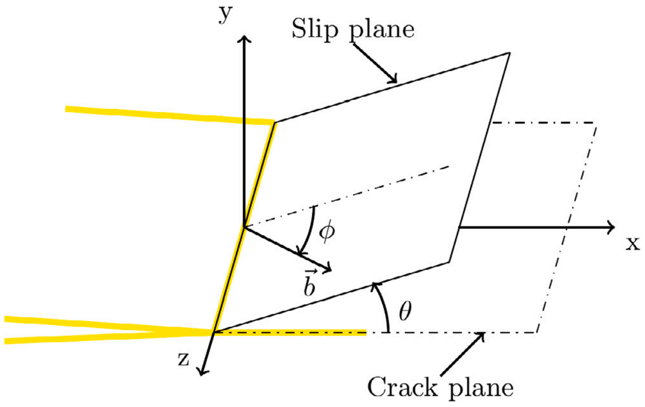

Fig. 1. Crack plane, slip system with slip direction $\vec{b}$ and angles θ and ϕ.

Tadmor et al. [95,96] introduced a criterion called twinnability, T, for the qualitative assessment of the twinning tendency of FCC and BCC materials, that is given as

$$T = \Gamma_{crit}\sqrt{\frac{\gamma_{us}}{\gamma_{ut}}}. \tag{8}$$

Here, γ_{ut} is the unstable twin energy, unique to slip system and twinning plane, and Γ_{crit} is the normalized nucleation load [95]. Following T, the stress intensity factor K_{IT} at which the nucleation of a twin is initiated can be evaluated as

$$K_{IT} = \frac{K_{IE}}{T} = \frac{K_{IE}}{\Gamma_{crit}}\sqrt{\frac{\gamma_{ut}}{\gamma_{us}}}, \tag{9}$$

where Γ_{crit} is equal to 1 for the case of BCC metals [21,86]. For the nucleation of a twin at the crack-tip, T generally needs to be larger than unity.

In addition to the above parameters, the stress intensity factor for plastic deformation, K_{pl}, can be defined as

$$K_{pl} = \min(K_{IE}, K_{IT}), \tag{10}$$

and the tendency for plastic deformation, T_{pl}, is evaluated using

$$T_{pl} = \frac{K_{pl}}{K_{IG}}, \tag{11}$$

for which ductile fracture is feasible if $T_{pl} < 1$ and brittle fracture occurs for $T_{pl} > 1$ [33,58,64].

4. Methods

4.1. Interatomic potentials

This study considers seven EAM potentials [28,97–102], herein referred to as EAM-1 to EAM-7, and two 2NN-MEAM potentials [54, 103], MEAM-1 and MEAM-2, of which the latter is fitted as part of this work. An overview of the fitting properties of the considered potentials is provided in Table 1. To the best of our knowledge, of the considered potentials only EAM-1 and MEAM-1 have been used for atomistic fracture studies of pre-cracks in tungsten [33,51,54,58,64, 104]. Since MEAM-1 exhibited substantial crack-tip blunting for single-crystal crack systems we employ the version in [54], which was slightly edited to circumvent such behaviour. All parameters were the same as for the original potential, except the cutoff and smoothing ranges that were increased to suppress the sharp peaks in the traction–separation curve that resulted in the crack-tip blunting, see [54]. Despite usage of the revised potential during the present study, we found that MEAM-1 exhibited some unusual double-sided crack branching for one of the GBs and prompted the development of a new 2NN-MEAM potential (MEAM-2), which also yields surface and unstable twinning energies that are in slightly better agreement with DFT data than MEAM-1. The details of the MEAM-2 fitting procedure and parametrization are provided in the supplementary material, section S1.

4.2. Bulk and defect modelling

For validation of the potentials, we performed molecular statics (MS) modelling of bulk and defect properties, and compared the outcomes with those from DFT calculations. For the MS simulations we used LAMMPS [105,106] and the DFT calculations were performed within the generalized gradient approximation (GGA) based on the PBE formalism [107,108]. To this end we used VASP [109–112], see supplementary material section S2 for details.

The elastic constants (C_{11}, C_{12} and C_{44}, at $T = 0$ K) were found by evaluating the strain energy for small strains. To characterize plastic yielding properties we investigated the generalized stacking fault energy (GSFE) and twinning energy curves. For the GSFE, we considered the {112} and {110} planes to study the energetics associated with slip for the Burgers vector, $\vec{b} = \frac{a}{2}\langle 111\rangle$. The atomic configuration was divided into two blocks – separated by the slip plane – that were incrementally translated relative to each other until the total distance of glide was equal to $\|\frac{a}{2}\langle 111\rangle\|$. For each increment, the atoms were allowed to relax in the normal-direction of the slip plane. Analogously, twin deformation profiles were modelled by sequentially shearing the parallel (112) planes incrementally up to the magnitude of the partial dislocation $\vec{b}_p = \frac{a}{6}\langle 111\rangle$, with subsequent atomic relaxation allowed in the twin normal direction. For the twinning curves there are two main symmetry configurations for the ground state configuration: isosceles and reflection structures [113]. Since DFT modelling has revealed the reflection configuration to be the most stable for tungsten [114], we considered it for the potential evaluation. In both MS and DFT, 30 atomic layers were used for GSFE and twinning curves.

To validate the brittle behaviour of the potentials, the traction–separation (TS) curves were studied along with the associated peak stress, $\sigma_{coh}^{(klm)}$, required to overcome the cohesive strength, and the maximum interaction range for traction, $\delta_{max,sep}^{(klm)}$. Since Nguyen and Ortiz [115] demonstrated that relaxation during separation of surfaces would lead to non-uniqueness in the TS behaviour, we limited ourselves to a static setup, with rigid separations for the present benchmark. The traction, σ, was calculated using the atomistic TS law, given by

$$\sigma(\delta) = \frac{1}{A}\frac{dE}{d\delta}, \tag{12}$$

where δ and A are the applied displacement and the cross-sectional area of the crystal, respectively.

The monovacancy energy was calculated by

$$E_{vac} = E_{N-1} - \frac{N-1}{N}E_N, \tag{13}$$

where E_{N-1} and E_N are the fully relaxed (i.e. both coordinate and cell relaxation) bulk energies with and without a vacancy, respectively. The total number of atoms, N, was chosen as 128 for both MS and DFT, which was sufficient to give converged results.

The surface energy associated with the (klm)-surface was obtained using

$$\gamma_{(klm)} = \frac{E_{fs} - N_{fs}\cdot E_{coh}}{2A_{fs}}, \tag{14}$$

where E_{fs}, N_{fs}, E_{coh} and A_{fs} are the energy of the system with free surfaces, number of atoms in the system with free surfaces, the cohesive energy and surface area, respectively. The surface energies were computed using MS by creating a slab with free boundary conditions in the surface normal direction and periodic boundary conditions in the in-plane directions, whereby the atomic coordinates were allowed to fully relax. The slab thickness was chosen to be large (>50 Å) to nullify the interactions between them. For the plane wave DFT modelling, an artificial vacuum interface in the surface normal direction of 12 Å was used to create the slab. The thickness of the slab was converged with respect to the surface energy and was chosen to be large (>20 Å) for well-converged results.

In general, coincidence site lattice (CSL) GBs are uniquely characterized by the inverse density of coincidence sites $\Sigma-$, the misorientation-angle, ψ, the adjoining crystallographic planes at the interface, $(klm)_1$ and $(npq)_2$, and the misorientation axis $[uvw]$. The herein considered symmetric tilt CSL GBs are provided in Table 2. They were generated by joining two identical grains and then rotating them about the rotation-axis such that angle between them corresponded to the misorientation-angle. To this end we utilized the code developed by Wojdyr et al. [116]. Because $(klm)_1$ and $(npq)_2$ are related for symmetric tilt GBs, for a more compact notation, henceforth only the $\Sigma-$ value and the GB plane $(klm)_1$ and, when necessary, the crack front direction are used to distinguish them.

The GB energy was calculated by

$$\gamma_{GB} = \frac{E_{GB} - N_{GB}\cdot E_{coh}}{2A_{GB}}, \tag{15}$$

where E_{GB} is the total energy of the simulation cell containing the GB, N_{GB} is the total number of atoms, A_{GB} is the area of the GB and the factor of 2 in the denominator is due to the simultaneous existence of two GBs in the simulation cell. To find the equilibrium ground state configuration of the GB, we probed different possible configurations by shifting one grain relative to the other in the GB plane and relaxing the atomic coordinates. The configuration that minimizes γ_{GB} was chosen as the equilibrium ground state configuration of the GB [62]. In the same manner as for the surface energy, the GB separation was chosen sufficiently large to avoid self-interaction, both in the MS and DFT modelling. Analogously to the single-crystal TS modelling, we evaluate the TS behaviour and peak stress, σ_{coh}^{GB}, for GBs.

Table 2
Herein studied CSL symmetric tilt GBs. ψ is the misorientation angle, $(klm)_1$ and $(npq)_2$ are the GB planes and $[uvw]$ is the misorientation axis.

Σ	ψ	$(klm)_1$	$(npq)_2$	$[uvw]$
3	109.5°	(111)	$(\bar{1}\bar{1}1)$	$[\bar{1}10]$
3	70.5°	(112)	$(\bar{1}\bar{1}2)$	$[\bar{1}10]$
5	36.9°	(310)	$(3\bar{1}0)$	[001]
9	38.9°	(114)	$(\bar{1}\bar{1}4)$	$[\bar{1}10]$
17b	86.6°	$(2\bar{2}3)$	$(\bar{2}23)$	$[\bar{1}10]$
17b	93.4°	$(3\bar{3}4)$	$(\bar{3}34)$	$[\bar{1}10]$

4.3. Fracture simulations

Quasi-static MS modelling was used to study cracks in single- and bicrystals subjected to mode I loading under plane strain conditions, see Fig. 2. The stress intensity-controlled loading was applied through utilization of the mode I displacement field, which is proportional to the stress intensity factor, K_I, and can be obtained from anisotropic linear elastic fracture mechanics as [87,88,117]:

$$u_x = \frac{K_I\sqrt{2r}}{\sqrt{\pi}}\Re\left\{\left[\frac{1}{(\mu_1-\mu_2)}\right]\left[\mu_1 p_2(\cos\theta+\mu_2\sin\theta)^{1/2} - \mu_2 p_1(\cos\theta+\mu_1\sin\theta)^{1/2}\right]\right\}, \tag{16}$$

$$u_y = \frac{K_I\sqrt{2r}}{\sqrt{\pi}}\Re\left\{\left[\frac{1}{(\mu_1-\mu_2)}\right]\left[\mu_1 q_2(\cos\theta+\mu_2\sin\theta)^{1/2} - \mu_2 q_1(\cos\theta+\mu_1\sin\theta)^{1/2}\right]\right\}, \tag{17}$$

where $\Re$ represents the real part operator, and

$$p_1 = s_{11}\mu_1^2 + s_{12} - s_{16}\mu_1,\ p_2 = s_{11}\mu_2^2 + s_{12} - s_{16}\mu_2,$$
$$q_1 = \frac{s_{12}\mu_1^2 + s_{22} - s_{26}\mu_1}{\mu_1},\ q_2 = \frac{s_{12}\mu_2^2 + s_{22} - s_{26}\mu_2}{\mu_2}. \tag{18}$$

The complex valued μ_1 and μ_2 were obtained by solving the characteristic equation

$$s_{11}\mu_j^4 - 2s_{16}\mu_j^3 + (2s_{12}+s_{66})\mu_j^2 - 2s_{26}\mu_j + s_{22} = 0, \tag{19}$$

where the compliance constants s_{ij}, which were evaluated at $T = 0$ K, were rotated to match the orientation of interest through suitable rotation operations.

The atomic configuration of the crack system of interest was generated in the form of a cylindrical single- (or bi) crystal system with the $x-$, $y-$ and $z-$directions representing crack propagation direction, the crack plane normal and crack front direction, respectively, see Fig. 2. Periodic boundary conditions were applied only in the z-direction, for which a cylinder thickness of ~40 Å was adopted. Based on a convergence study of the variation of the computed critical stress intensity factor, K_I^{crit}, for a brittle GB crack system, the cylinder radius was chosen as ~160 Å, see Figure S1 in section S3 of the supplementary material.

To implement the displacement-controlled loading, we utilized hybrid stress border conditions [117] concurrently with the anisotropic displacement field. To this end, the cylinder was divided into two regions: inside and boundary regions, which were concentric at the crack-tip. The inside region, which was contiguous with the boundary region and comprises the atoms of the process zone that were free to

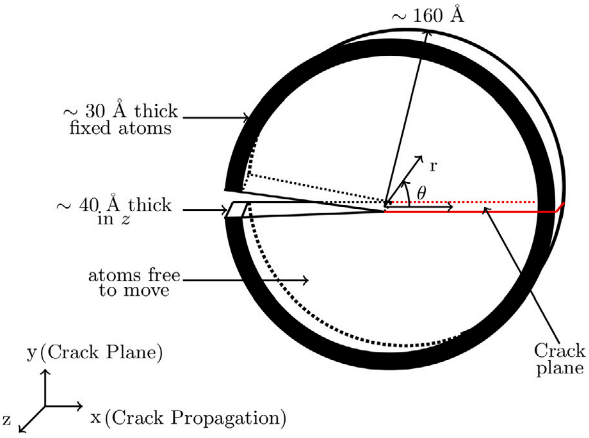

Fig. 2. Crack simulation setup in 3D.

relax, extended radially for about 130 Å from the crack-tip. The thickness of the outer region, which contained the rigidly displaced atoms to effectuate the mode I displacements, was chosen as approximately 30 Å. This is significantly (more than five times) larger than the cutoff range of the potentials.

Under loading, the atomic positions were updated relative to the crack-tip by incrementally applying the anisotropic displacement field given by Eqs. (16)–(17) in the x–y plane, in stress intensity factor increments, δK. In our simulations, we have used the increment $\delta K = 0.025$ MPa m$^{1/2}$, which is the error bar in the computed fracture toughness. After every update of the displacement field, the energy of the system was minimized through the use of the conjugate gradient algorithm to update the positions of the free atoms. Throughout the simulation the atoms that were separated by the initial crack (i.e. for $x < 0$ see Fig. 2) were prevented from interacting with each other. Other than that was none of the interatomic interaction altered or prescribed. This ensured that the conditions for crack opening and closure remained equal, such that lattice/bond trapping could be consistently computed.

Cracks in bicrystals were set up similar to the single-crystals, except that the two single-crystals with different orientations were merged such that a GB formed where they met. Although we did account for elastic anisotropy and the different orientations of both grains when applying the displacement field, owing to the inherent isotropy of tungsten such effects were found to be small.

5. Results

5.1. Bulk and defect properties

This section provides a comparison of different interatomic potentials for the evaluation of bulk and defect properties. All raw data is presented in Tables S2 and S3 of section S4 in the supplementary material.

5.1.1. Elastic constants, surface and vacancy energies

With regards to elastic moduli, a very good agreement with the experimental data is observed, except for the slightly higher C_{44} value of MEAM-2, see Fig. 3. This deviation is a consequence of adjusting the 2NN-MEAM parameter β_0 (see [103]) so that C_{11} and C_{12} values agree better with DFT and experimental data.

In agreement with the DFT calculations, all the potentials give the close packed/high density (110) surface as the lowest energy surface. But in contrast to our DFT calculations, as well as prior DFT works [118, 119] that produced surface energies with the order $\gamma_{(100)} > \gamma_{(111)} > \gamma_{(112)} > \gamma_{(110)}$, the surface energies are ordered as $\gamma_{(111)} > \gamma_{(112)} > \gamma_{(100)} > \gamma_{(110)}$ for all EAM potentials and MEAM-1. Unlike these potentials, MEAM-2 shows the following order: $\gamma_{(111)} > \gamma_{(100)} > \gamma_{(112)} > \gamma_{(110)}$, suggesting that at least the relative order of the two lowest energy surfaces considered is captured although it is noted that $\gamma_{(100)}$ and $\gamma_{(112)}$ are almost degenerate.

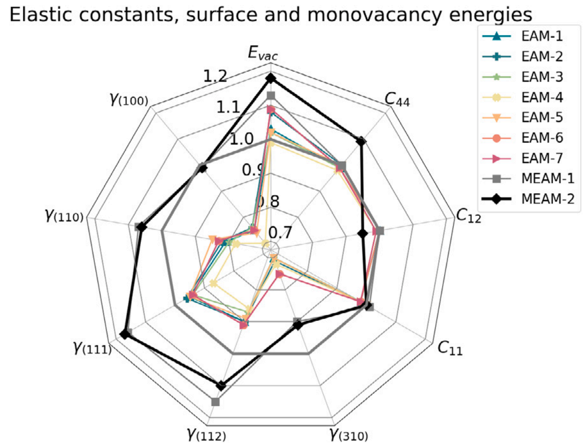

Fig. 3. Performance of potentials in predicting elastic constants, surface and monovacancy formation energies. Here, all values have been normalized with respect to herein calculated DFT data, except elastic constants that are normalized with respect to respective experimental values. The solid grey grid line corresponds to value 1.0. The data is provided in the supplementary material, see Table S2 therein.

Among all potentials MEAM-1 and MEAM-2 are the only ones that consistently predict surface energy data of similar magnitude to that of DFT, see Fig. 3. The most significant deviation from DFT is found for $\gamma_{(111)}$, which both MEAM-1 and MEAM-2 overestimate by ~17%, whereas the EAM potentials generally underestimate the surface energy by up to 30%.

Most of the potentials underestimate the surface energies because, when they are fitted to the vacancy formation energy as the only low coordinated configuration, typically the slope of the background electron density for the surface atoms is not captured [26]. This suggests that, in general, there will be a trade-off between E_{vac} and surface energy, depending on the fitting dataset. In our case, this is illustrated by the fact that MEAM-2 overestimates the vacancy formation energy, while that of the EAM potentials deviate by up to 10% from DFT data, see Fig. 3.

5.1.2. Generalized stacking fault and twinning energies

The GSFE curves for {112} and {110} planes along the ⟨111⟩ direction are presented in Fig. 4. Except for EAM-2, a single well-defined energy peak, i.e., the unstable stacking fault energy γ_{us}, is observed for all the potentials. The EAM-2 GSFE curves exhibit two peaks indicating a stable stacking fault. Such a stable stacking fault is feasible only when there is an intersection of two non-parallel symmetric planes with the glide plane of the crystal [120]. In general, BCC materials do not show stable stacking faults because there are no such intersections [121]. Along these lines, Möller et al. [122] showed that the emergence of a stable stacking fault in BCC metals by empirical interatomic potentials is an artefact, as DFT and bond-order potentials do not give rise to such behaviour — even under strained conditions.

DFT data for γ_{us} is well reproduced by EAM-4, EAM-6, EAM-7, MEAM-1 and MEAM-2, with less than 10% deviation. Compared with the reference DFT data, γ_{us} is significantly underestimated by EAM-1 and EAM-3, whereas it is severely overestimated by EAM-2. Similar tendencies are seen for the (112)[11$\bar{1}$] slip system, although we note that all potentials are found to be symmetric around $\|\vec{b}/2\|$, while the GSFE curve derived from DFT the peak is slightly perturbed to an off-centre position at about $0.6\|\vec{b}\|$. These findings are in accordance with DFT results in [118].

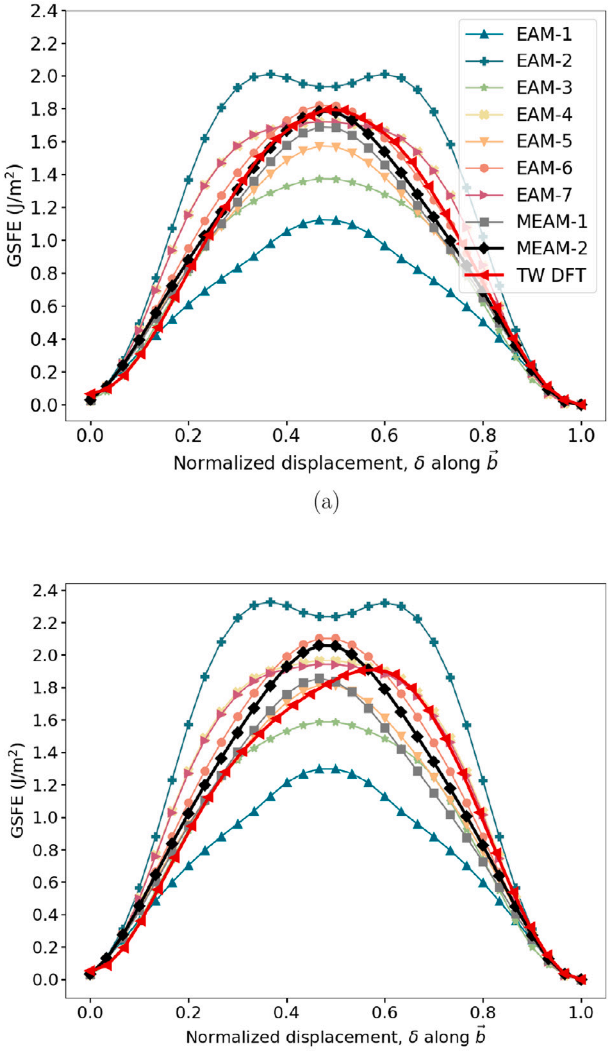

(a)

(b)

Fig. 4. Comparison of generalized stacking fault energy in (a) (110)$[1\bar{1}1]$ and (b) (112)$[11\bar{1}]$ faults with DFT data. Here, $\vec{b} = \frac{a}{2}\langle 1\bar{1}1\rangle$ is the Burgers vector.

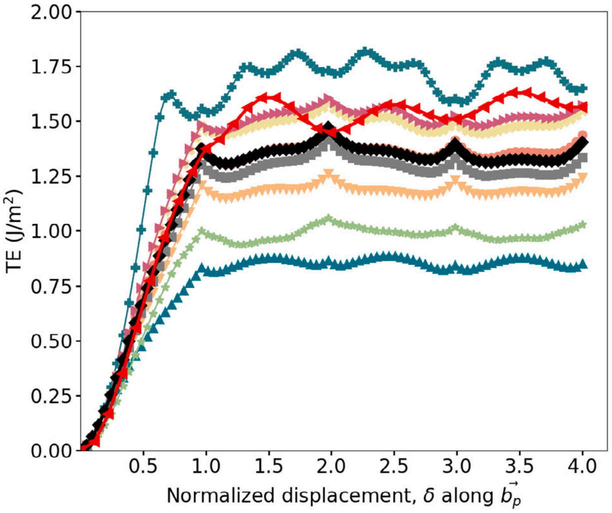

Fig. 5. (112)$[11\bar{1}]$ twinning energy pathway comparison with DFT data computed in This Work. Here $\vec{b_p}$ corresponds to $\frac{a}{6}[11\bar{1}]$. The markers correspond to those in Fig. 4.

From the twinning energy pathways shown in Fig. 5, it is evident that the DFT energy peaks and troughs are different from those of the classical potentials. We find that the DFT maxima coincide with the minima of the empirical potentials and vice versa. Such out-of-phase behaviour has been previously reported in the literature [113,123], which suggests that the empirical potentials do not reproduce the perfect reflection twin structure to be the most stable. Instead, the ground-state structure is likely a configuration that lies somewhere between the perfect reflection and isosceles structures, which is a common trait for empirical potentials designed for BCC transition metals [113]. Notably, EAM-4, EAM-6, EAM-7 and MEAM-2 predict an unstable twinning energy that deviates by less than 10% from the DFT data. With the exception of EAM-2, which overestimates γ_{ut}, the remaining potentials underestimate it by up to ~40%.

5.1.3. Traction–separation behaviour of single-crystals

The DFT calculations show that the curve of traction as a function of rigid separation is smooth and positively skewed bell-shaped in nature, with a single, well-defined maximum, see Fig. 6. In the following, such TS behaviour is referred to as well-behaved.

Only the EAM-1, EAM-5, EAM-6, MEAM-1 and MEAM-2 potentials show such well-behaved TS curves for the (100), (110), (111) and (112) cleavage planes. These are shown together with our DFT results in Fig. 6. The remaining EAM potentials showed artefacts such as multiple local maxima, negative stress regions or significant oscillatory behaviour. Their TS curves are available in Figure S2 in section S4 of the supplementary material.

In general, the peak stresses, $\sigma_{coh}^{(klm)}$, of MEAM-1 and MEAM-2 are comparable to DFT with less than 10% deviation, see Fig. 7. For the EAM-1 potential, only $\sigma_{coh}^{(111)}$ and $\sigma_{coh}^{(112)}$ are comparable to DFT. The remaining potentials overestimate the peak stresses, where the most notable discrepancy with DFT data is found for $\sigma_{coh}^{(111)}$, which ranges from ~20% up to more than 100%.

The maximum interaction range, $\delta_{max,sep}^{(klm)}$, for the TS curves also varies, see Fig. 7. The DFT calculations suggest an interaction distance between 4.0 to 5.0 Å, which is significantly underestimated by most EAM potentials, see Fig. 7. Besides exhibiting the highest peak stresses, EAM-2 has the shortest interaction range, which is less than half of that predicted by DFT. Thus it exhibits a very steep downhill post-peak stress behaviour. For the MEAM potentials, the interaction range underestimate the DFT data by ~20%.

5.1.4. Grain boundary properties

According to DFT studies in [5,62], the $\Sigma5,(310)[001]$ GB is the only one of the considered GBs that during relaxation undergoes an in-plane shift along the misorientation axis. The DFT calculations predict a shift between 1/6 and 1/4 times a_0 along the [001]-direction [62]. However, this is not captured by any of the potentials herein. From Fig. 8(a), it follows that the capability of the potentials to reproduce the DFT grain boundary energies according to the literature [62] varies significantly. The only potentials that consistently have GB energies comparable to DFT are EAM-6, MEAM-1 and MEAM-2, which deviate by less than 10% from DFT data [62]. Owing to the low surface energies for most EAM potentials, the ideal energy release rate (also ideal work of separation, Eq. (5)) is also generally underestimated, see Fig. 8(b). In contrast, the corresponding data computed with MEAM-1 and MEAM-2 agree well with DFT data.

The TS curves and peak stresses for the rigid interfacial separation of a low energy ($\Sigma3,(112)[1\bar{1}0]$) and a high energy ($\Sigma5,(310)[001]$) GB are shown in Fig. 9(a) and (b), respectively, for the same selected potentials as in Fig. 6 (TS curves for the remaining potentials are shown in Figure S3 in section S4 of the supplementary material). The smooth and positively skewed bell-shaped profile of the TS curves from our DFT calculations is recovered for both GBs only by MEAM-1, MEAM-2 and EAM-5. The best agreement in terms of peak stress is found for EAM-1, MEAM-1 and MEAM-2, which deviate by less than ~ 15% from DFT data, see Fig. 9(c) and (d) .

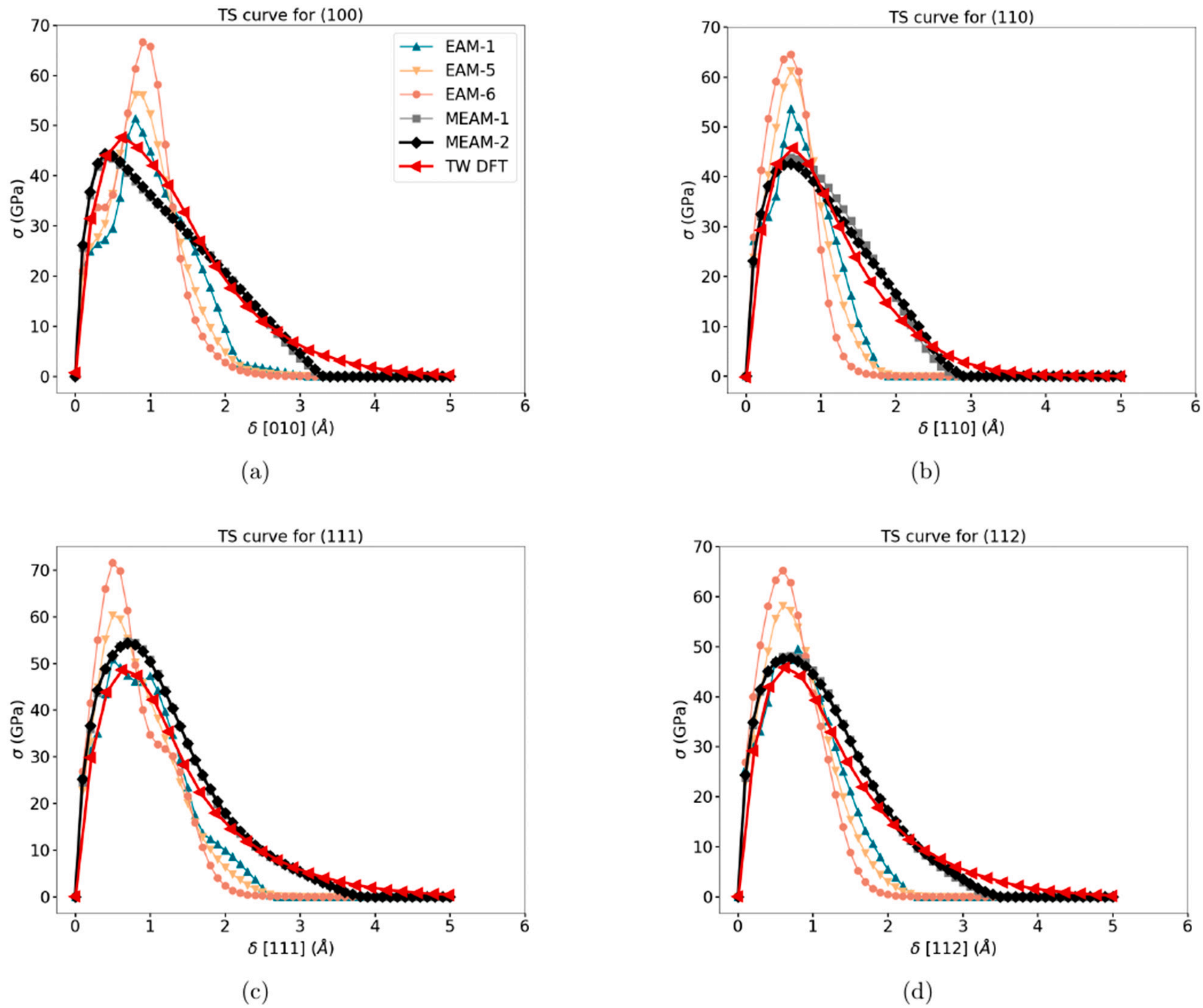

(a) (b)

(c) (d)

Fig. 6. Comparison of TS curves of (a) (100) (b) (110) (c) (111) and (d) (112) surfaces with DFT data computed in This Work. Here, δ is the separation distance. Only EAM potentials that do not show strong artefacts are included, the excluded TS curves are shown in Figure S2 in the supplementary material.

5.2. Single-crystal fracture

The computationally determined K_I^{crit} as well as the different crack-tip mechanisms that take place are summarized together with the lattice trapping ΔK in Table 3 for the nine single-crystal crack systems: $(001)[0\bar{1}0]$, $(001)[1\bar{1}0]$, $(110)[\bar{1}10]$, $(01\bar{1})[\bar{1}00]$, $(111)[11\bar{2}]$, $(111)[1\bar{1}0]$, $(112)[\bar{1}10]$, $(114)[1\bar{1}0]$ and $(\bar{1}\bar{1}5)[1\bar{1}0]$.

For cracks on $\{100\}$ and $\{110\}$, most potentials show brittle crack advancement along the initial crack planes, which are the preferred cleavage planes of tungsten, see Table 3. An exception to this behaviour is seen for the $(001)[0\bar{1}0]$ crack system, where crack deflection onto the (101) plane is observed for most instances, see Fig. 10(a). Only EAM-5 and EAM-6 showed the emission of an edge dislocation on the (110) plane with Burgers vector $\frac{a}{2}[\bar{1}11]$ from the $(110)[\bar{1}10]$ crack-tip, while the potentials by Marinica et al. [28] (EAM-4 and EAM-7) exhibited continued crack propagation along the initial (001) plane. Additionally, a phase transformation of the crack-tip and surrounding region is observed for EAM-2, see Fig. 10(b). Such transformations are accompanied with high critical stress intensity factors, and for the $(01\bar{1})[\bar{1}00]$ system, it is seen not only for EAM-2, but also for the EAM-3 potential. This type of behaviour has been observed previously in atomistic simulations of α-Fe [126], and is believed to be an artefact of the potential.

For all systems where the crack propagation proceeds in a brittle manner along the initial crack plane, see Fig. 10(c), we compute the lattice trapping. Although large variations are encountered for the different potentials, see Table 3, some general tendencies can be observed. Interestingly, we find that the MEAM potentials have lattice trapping ranges that are significantly smaller than the EAM potentials. Moreover, the general trend is that lower lattice trapping is obtained for cracks with $\langle 110\rangle$ fronts than for $\langle 100\rangle$ crack fronts. Such differences are responsible for the previously observed crack front anisotropy for cracks on the same cleavage plane, but with different crack front orientations [38,125].

While most potentials exhibit dislocation emission for $(111)[11\bar{2}]$ cracks, see Fig. 10(d), the Marinica potentials give rise to brittle crack propagation. The nucleated dislocations have the Burgers vector $\vec{b} = \frac{a}{2}[111]$ and glide on the $(\bar{1}10)$ plane. For the $(111)[1\bar{1}0]$ cracks, the emission of twins is observed for most potentials. This is in agreement with the atomistic results in [58], in which EAM-1 was also employed. Deviations from this behaviour is seen for EAM-3, which undergoes dislocation emission, and for the Marinica potentials, where brittle fracture ensues on the $(22\bar{1})$ plane.

The failure of the $(112)[\bar{1}10]$ crack system is characterized by twin formation (see Fig. 10(e)) by most potentials. Notable exceptions are EAM-2, which undergoes crack-tip transformation, and the Marinica potentials, which again behave in a brittle manner.

Table 3

Computed K_I^{crit} (in units of MPa m$^{1/2}$) and ΔK for single-crystal crack systems. In the following, B, D, T and CTT correspond to brittle, dislocation emission, deformation twin formation and the crack-tip transformation associated with brittle growth, respectively. The notation B$^{(klm)}$ represents deflected brittle crack propagation onto the (klm)-plane. ΔK is not computed for B$^{(klm)}$, B+CTT, T and D. Lack of experimental data in the table reflects unavailability of corresponding reference data in [38,125].

Crack system	EAM-1			EAM-2			EAM-3			EAM-4			EAM-5		
	K_I^{crit}	Event	ΔK	K_I^{crit}	Event	ΔK	K_I^{crit}	Event	ΔK	K_I^{crit}	Event	ΔK	K_I^{crit}	Event	ΔK
$(001)[0\bar{1}0]$	2.35	B$^{(10\bar{1})}$	–	3.93	B+CTT	–	2.28	B$^{(101)}$	–	1.21	B	0.33	2.90	B$^{(10\bar{1})}$	–
$(001)[1\bar{1}0]$	1.92	B	0.19	2.95	B+CTT	–	1.78	B	0.18	1.13	B	0.18	1.98	B	0.23
$(110)[\bar{1}10]$	1.91	B	0.23	3.23	B+CTT	–	1.90	B	0.29	1.03	B	0.32	1.98	D	–
$(01\bar{1})[\bar{1}00]$	2.58	B	0.91	3.23	B+CTT	–	2.70	B+CTT	–	1.53	B	1.44	2.63	B	1.14
$(111)[11\bar{2}]$	1.95	D	–	3.10	D	–	2.03	D	–	1.25	B	0.32	2.65	D	–
$(111)[1\bar{1}0]$	1.90	T	–	3.70	T	–	2.45	D	–	1.28	B$^{(22\bar{1})}$	–	2.03	T	–
$(112)[\bar{1}10]$	1.71	T	–	2.93	B+CTT	–	2.00	T	–	1.20	B	0.55	2.13	T	–
$(114)[1\bar{1}0]$	1.78	T	–	3.33	B$^{(110)}$+CTT	–	2.18	T	–	1.30	B$^{(110)}$	–	2.20	B$^{(110)}$+CTT	–
$(\bar{1}\bar{1}5)[1\bar{1}0]$	1.75	T	–	2.88	B$^{(111)}$+CTT	–	2.08	T	–	1.23	B$^{(111)}$	–	2.03	B$^{(111)}$+CTT	–
	EAM-6			EAM-7			MEAM-1			MEAM-2			Expt (77 K) [38,125]		
	K_I^{crit}	Event	ΔK	K_I^{crit}	Event	ΔK	K_I^{crit}	Event	ΔK	K_I^{crit}	Event	ΔK	K_I^{crit}	Event	ΔK
$(001)[0\bar{1}0]$	2.07	B$^{(10\bar{1})}$	–	1.63	B	0.51	2.03	B$^{(10\bar{1})}$	–	2.13	B$^{(10\bar{1})}$	–	3.4 ± 0.6	B	–
$(001)[1\bar{1}0]$	2.23	B	0.48	1.33	B	0.15	2.05	B	0.09	1.95	B	0.04	2.4 ± 0.4	B	–
$(110)[\bar{1}10]$	2.28	D	–	1.78	B	0.24	1.83	B	0.03	1.70	B	0.03	2.8 ± 0.2	B	–
$(01\bar{1})[\bar{1}00]$	3.15	B	1.31	1.73	B	1.30	2.28	B	0.36	2.13	B	0.25	3.8 ± 0.4	B$^{(100)}$	–
$(111)[11\bar{2}]$	2.90	D	–	1.50	B	0.28	2.33	D	–	2.35	D	–	–	–	–
$(111)[1\bar{1}0]$	2.30	T	–	1.48	B$^{(22\bar{1})}$	–	2.20	T	–	2.10	T	–	9.2 ± 0.6	B^{unknown}	–
$(112)[\bar{1}10]$	2.15	T	–	1.43	B	0.39	2.13	T	–	2.00	T	–	7.8 ± 0.9	B$^{(100)}$	–
$(114)[1\bar{1}0]$	1.65	T	–	1.53	B$^{(110)}$	–	2.1	B$^{(110)}$	–	2.03	B$^{(110)}$	–	–	–	–
$(\bar{1}\bar{1}5)[1\bar{1}0]$	2.45	T	–	1.43	B$^{(111)}$	–	2.08	B$^{(111)}$	–	1.98	B$^{(111)}$	–	–	–	–

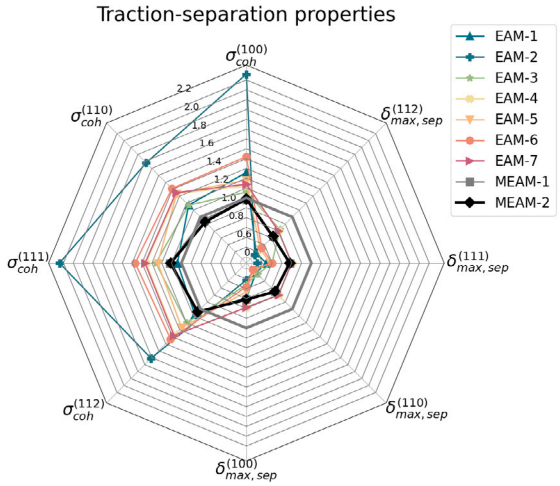

Fig. 7. Performance of potentials in predicting traction–separation properties. Here, all values have been normalized with respect to herein calculated DFT data. The solid grey grid line corresponds to value 1.0. The data is provided in the supplementary material, see Table S2 therein.

For cracks on the {114} and {115} planes, the majority of the potentials give rise to a brittle behaviour, with the cracks deflecting onto {110} and {111} planes, respectively, see Fig. 11. Only EAM-1, EAM-3 and EAM-6, which exhibit twin formation, reproduce the atomistic results in [58], while crack-tip transformation was seen for EAM-2 and EAM-5.

5.3. Grain boundary fracture

Grain boundary fracture was only studied with potentials that produced artefact-free single-crystal TS curves, i.e., EAM-1, EAM-5, EAM-6, MEAM-1, and MEAM-2. We studied the selected GBs in Table 2 and for the $\Sigma3,(111)[1\bar{1}0]$, $\Sigma3,(112)[1\bar{1}0]$ and $\Sigma5,(310)[001]$ GBs, we also considered different crack propagation directions to highlight the directional impact on different failure mechanisms. The fracture toughness values and bond trapping ranges of these cracks are provided in Table 4.

For all considered EAM potentials, the fracture behaviour of the $\Sigma3,(111)[1\bar{1}0]$ GB is highly sensitive to the crack propagation direction, in agreement with observations from [33], in which EAM-1 was used. This is illustrated by the occurrence of twinning when the crack propagates in the $[\bar{1}\bar{1}2]$-direction and brittle fracture in the opposite direction, see Fig. 12, for which the former generally exhibits the highest K_I^{crit} value. This is attributed to three jointly contributing mechanisms. First, the breakage of crystallographic symmetry for GBs, which may limit the accessibility to slip planes and trigger different mechanisms in different crack propagation directions [33,127,128]. Second, the inherent twinning and anti-twinning directional asymmetry in BCC metals [19,129,130], which can contribute to different responses, and, finally, varying bond trapping at the crack-tip in the different directions, due to asymmetric GB structural units. Similar tendencies are observed for the $\Sigma3,(112)[1\bar{1}0]$ GB, albeit only for EAM-1. Contrary to the EAMs, the MEAM potentials give rise to brittle fracture behaviour along both propagation directions for the $\Sigma3$ GB cracks. For these crack systems, our general observation is that the observed bond trapping is lower for MEAM potentials than for EAM potentials, which is similar to the findings in the single-crystal case.

From Table 4, it is clear that especially the EAM potentials give rise to some instances of crack-tip transformation. In the same manner as for single-crystal systems, the K_I^{crit} values associated with such behaviour are generally high. For the MEAM-1 potential, we observe an unusual double branching for the $\Sigma5,(310)[001]$ GB, which is accompanied by local transformation at the crack-tip. In this case the branched cracks propagate on {110} planes and diverge from the GB, see Fig. 12(c). Admittedly, we did observe such behaviour for the early-stage potential during the fitting of MEAM-2. But we found that by editing the potential such that the force required to separate an adatom from a {110} surface was slightly reduced, the transformation and branching disappeared for the benefit of brittle crack propagation. Thus, instead the final MEAM-2 version predicts brittle crack propagation along the GB, at which it forms {110} facets, see Fig. 12(d).

Consistent with the results in [64], which was based on EAM-1, the considered cracks in $\Sigma9,(114)[1\bar{1}0]$ GBs are brittle in nature according to all potentials. For the $\Sigma17b$ GBs, twinning is observed for all employed EAM potentials, while brittle failure occurs for the MEAM potentials. For MEAM-2, we note remarkably high K_I^{crit} and ΔK associated with brittle failure of $\Sigma17b,(2\bar{2}3)[110]$.

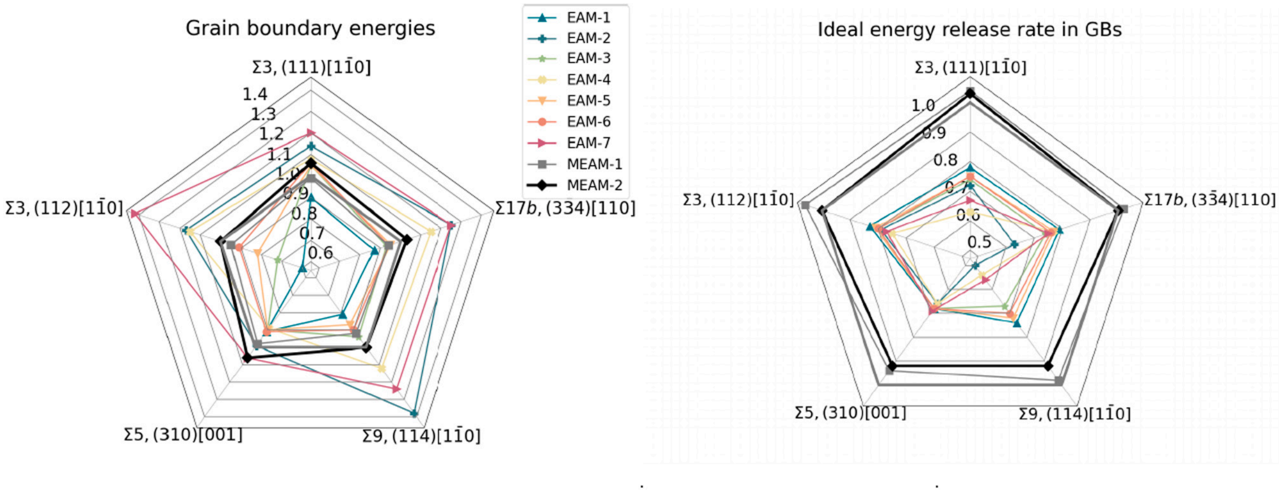

(a) (b)

Fig. 8. Comparison of (a) GB energies, γ_{GB} and (b) ideal energy release rate, G_I^{GB} (Eq. (5)) obtained from MEAM and EAM potentials with DFT data in [62]. The solid grey grid line corresponds to value 1.0.

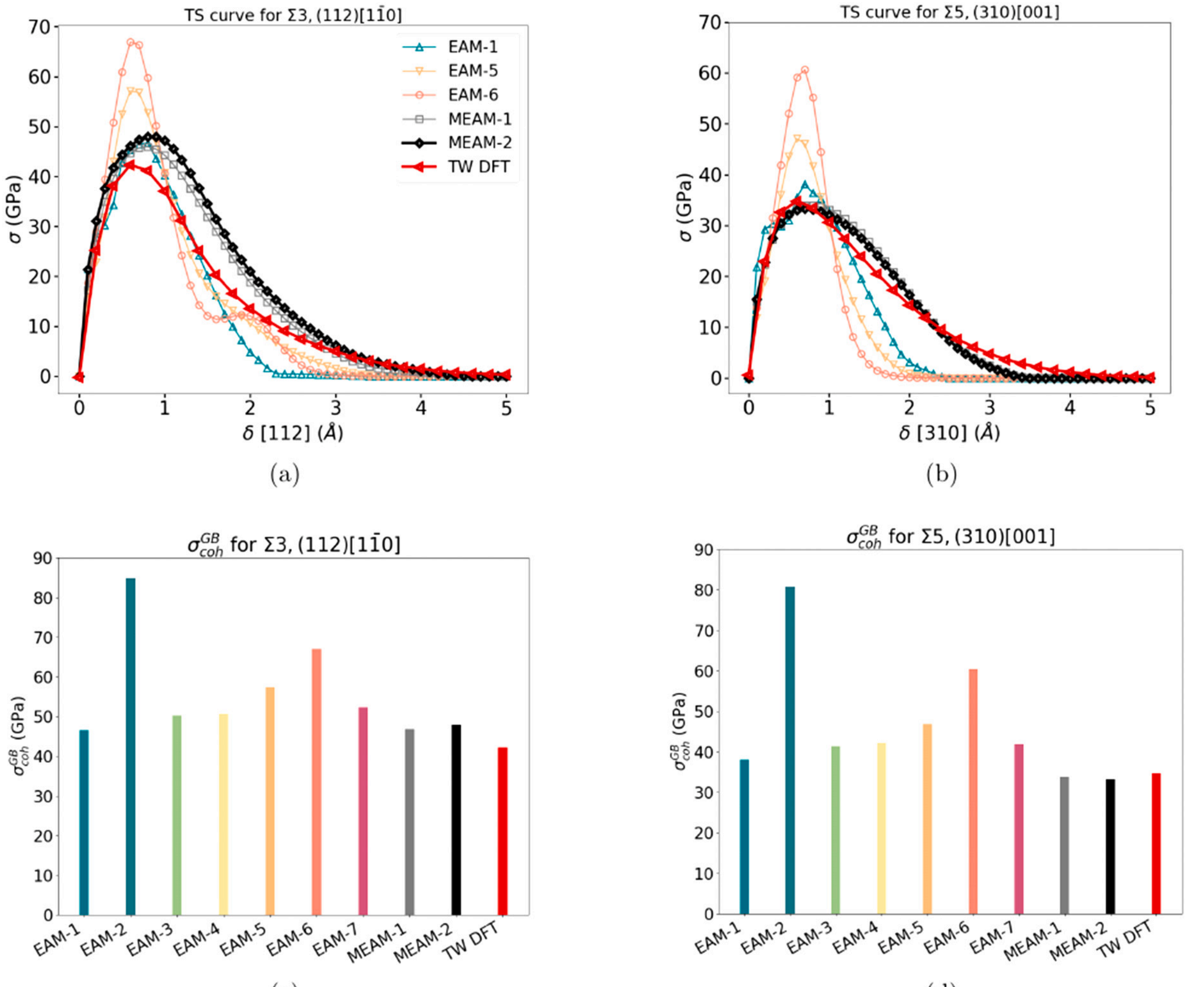

(c) (d)

Fig. 9. Comparison of TS curves of (a) $\Sigma 3$,(112)[1$\bar{1}$0] and (b) $\Sigma 5$,(310)[001] GBs with DFT data. Here, δ is the separation distance. Only EAM potentials that do not show strong artefacts are included, the excluded TS curves are shown in Figure S3 in the supplementary material. In (c) and (d), cohesive strength σ_{coh}^{GB} of GBs obtained from MEAM and EAM potentials is compared with DFT data in this work.

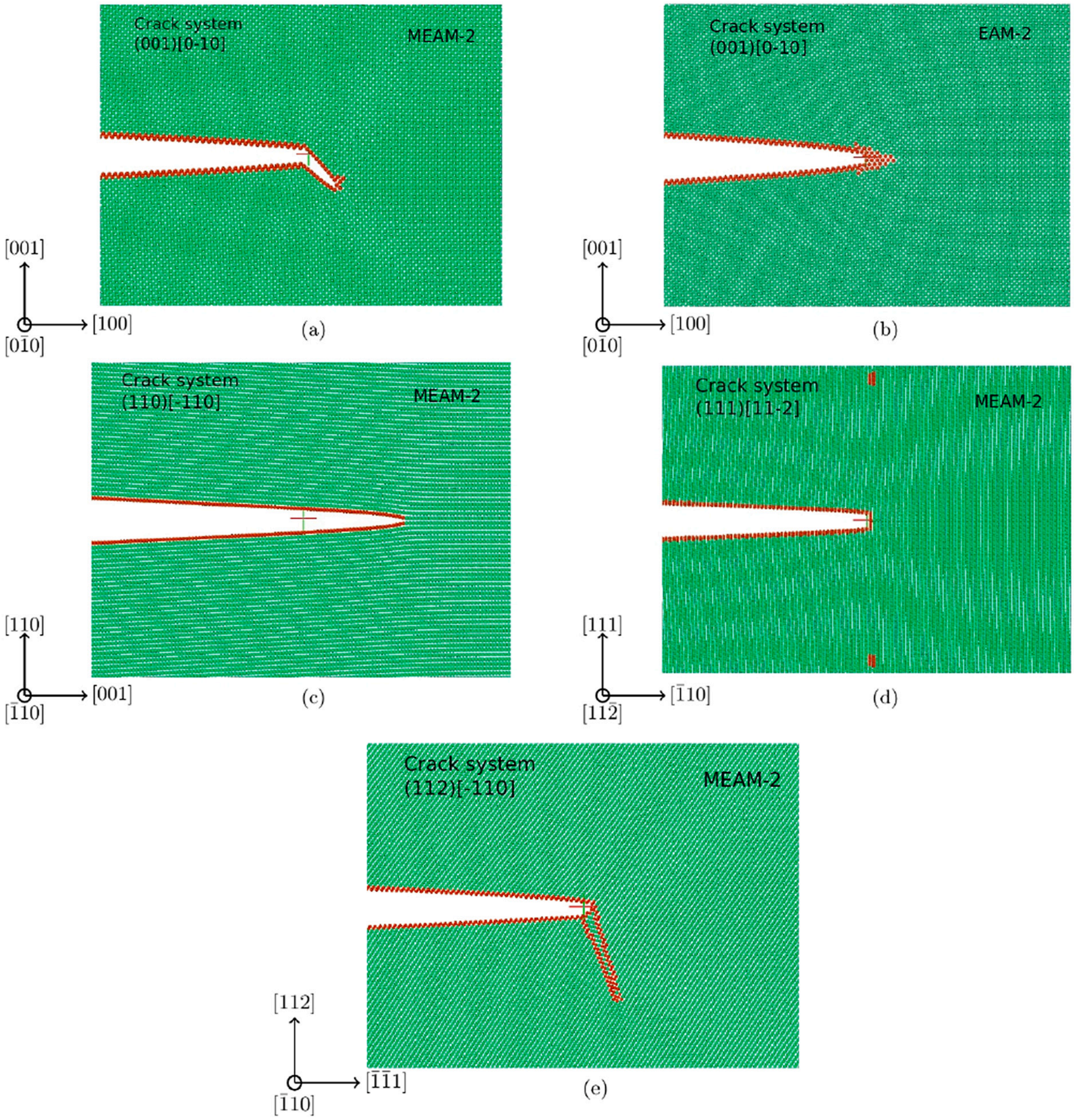

Fig. 10. Simulation snap shots illustrating different possible crack-tip mechanisms: (a) $(001)[0\bar{1}0]$ crack growth on (110) plane, (b) crack-tip transformation in $(001)[0\bar{1}0]$ crack system, (c) cleavage of the $(110)[\bar{1}10]$ crack on the initial plane, (d) dislocation emission in $(111)[11\bar{2}]$ and (e) twin formation in $(112)[\bar{1}10]$ crack systems. The atoms are coloured based on common neighbour analyses [124], where green particles represent BCC-coordinated atoms and red ones are non-BCC atoms. '+' indicates the origin (0,0), which is the initial crack-tip position.

Table 4
Computed K_I^{crit} (in units of MPa $m^{1/2}$) and ΔK for cracks in bicrystal systems. B and T are the short forms for brittle crack growth on initial plane and twin formation. CTT and DBr+CTT indicate the crack-tip transformation associated with brittle growth and double branching followed by crack-tip transformation, respectively. ΔK is not computed for B+CTT, DBr+CTT and T. "pr.dir" refers to crack propagation direction.

GB, crack system	EAM-1			EAM-5			EAM-6			MEAM-1			MEAM-2		
Σ,(plane)[front][pr.dir]	K_I^{crit}	Event	ΔK	K_I^{crit}	Event	ΔK	K_I^{crit}	Event	ΔK	K_I^{crit}	Event	ΔK	K_I^{crit}	Event	ΔK
$\Sigma3,(111)[1\bar{1}0][\bar{1}\bar{1}2]$	1.63	T	–	1.85	T	–	1.93	T	–	1.40	B	0.27	1.30	B	0.13
$\Sigma3,(111)[1\bar{1}0][11\bar{2}]$	1.43	B	0.24	1.20	B	0.46	1.45	B	1.42	1.25	B	0.07	1.20	B	0.23
$\Sigma3,(112)[1\bar{1}0][\bar{1}\bar{1}1]$	1.38	T	–	1.75	B+CTT	–	2.48	B+CTT	–	1.38	B	0.08	1.53	B	0.22
$\Sigma3,(112)[1\bar{1}0][11\bar{1}]$	1.71	B	0.48	1.65	B	0.38	1.80	B+CTT	–	1.61	B	0.22	1.38	B	0.12
$\Sigma5,(310)[001][1\bar{3}0]$	1.60	B	1.03	2.05	B+CTT	–	2.95	B+CTT	–	1.90	DBr+CTT	–	1.85	B	0.21
$\Sigma5,(310)[001][\bar{1}30]$	2.28	B+CTT	–	3.13	B+CTT	–	4.13	B+CTT	–	1.61	B	0.13	1.73	B	0.11
$\Sigma9,(114)[1\bar{1}0][22\bar{1}]$	1.70	B	0.48	1.55	B	0.90	1.88	B	2.13	1.35	B	0.42	1.63	B	0.36
$\Sigma17b,(2\bar{2}3)[110][3\bar{3}\bar{4}]$	1.63	T	–	1.93	T	–	2.13	T	–	1.50	B	0.17	1.98	B	1.08
$\Sigma17b,(3\bar{3}4)[110][\bar{2}23]$	1.75	T	–	1.85	T	–	2.15	T	–	1.43	B	0.09	1.65	B	0.47

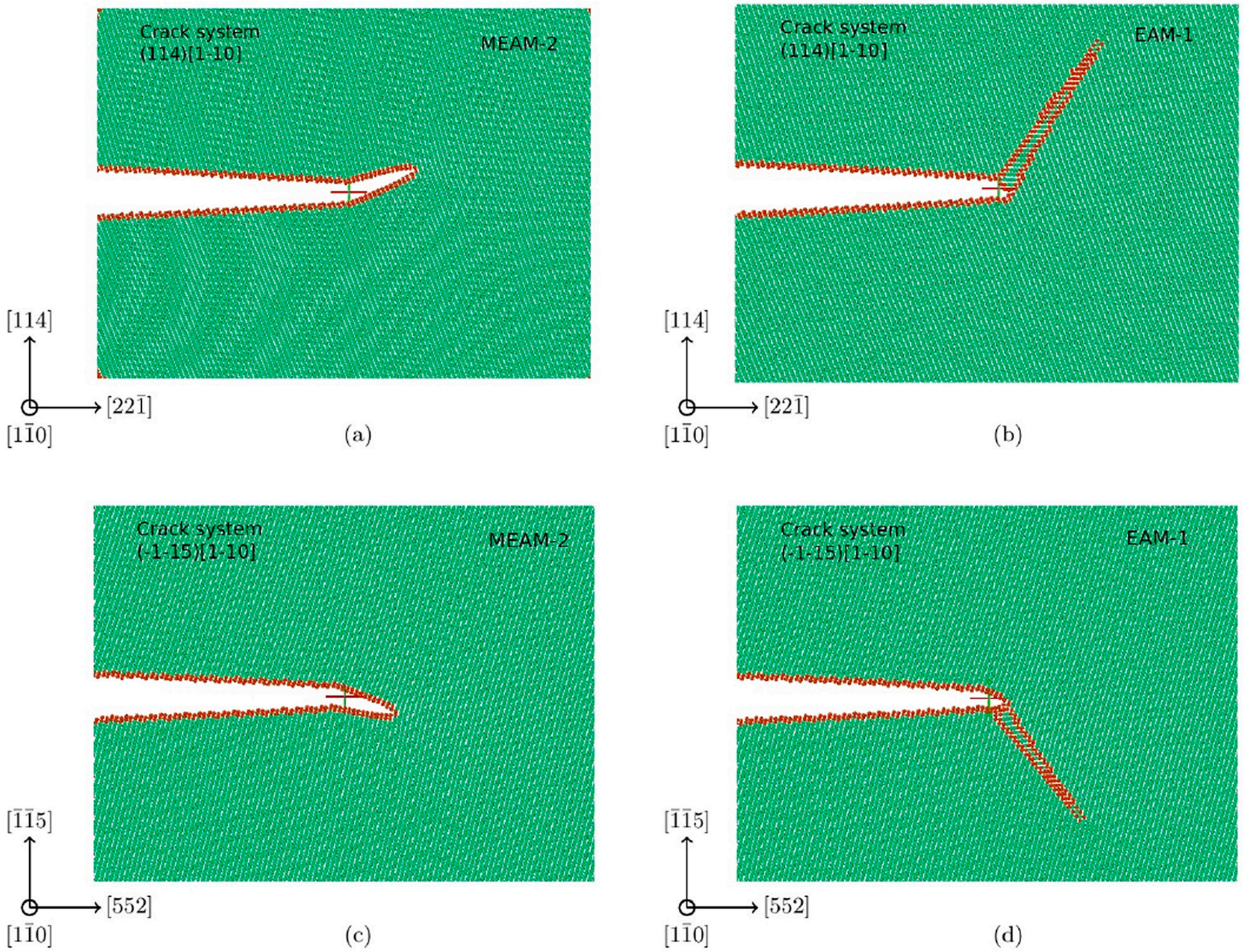

Fig. 11. Evolution of crack in (114)[1$\bar{1}$0] crack system using (a) MEAM-2 (b) EAM-1 and crack in ($\bar{1}\bar{1}$5)[1$\bar{1}$0] using (c) MEAM-2 (d) EAM-1. The particle colouring corresponds to that in Fig. 10. '+' is the origin (0,0) which is the initial crack-tip position.

6. Discussion

6.1. Fracture properties and behaviour

Theoretical predictions based on Griffith's and Rice's models project brittle fracture to ensue for all crack systems and potentials (see Tables S4 and S5 in section S5 of the supplementary material for theoretical predictions of the critical stress intensity factor). But from the results it is clear that different potentials in general give rise to very different fracture behaviour and the resulting critical stress intensity factor varies.

By exploiting the elastic isotropy of tungsten and the computed surface and grain boundary energies of the potentials, in Fig. 13(a) and (b) we compare the analytical Griffith fracture toughness with the atomistic counterparts for single-crystals and GBs, respectively.

In general, it is seen that the atomistic data is scattered around the analytical fracture toughness for both cases. Despite being a thermodynamic lower limit for single-crystals, some of the data points for brittle fracture toughness of single-crystals computed using EAM-4 and EAM-7 are below the theoretical Griffith's fracture toughness, see Fig. 13(a). This is believed to be a consequence of the oscillatory TS behaviour with multiple local minima produced by those potentials (see Figure S3 in the supplementary material), which may manifest in intermediate stages in the bond-breaking process that can lead to underestimation of the fracture toughness.

Unlike single-crystals, the structural units of GBs lead to a crack-tip position dependence of the bond trapping and thus also of the fracture toughness [33]. This can manifest itself in values for the brittle fracture toughness below the theoretical Griffith estimate as, e.g., apparent in the points below the theoretical line in Fig. 13(b).

Systems that undergo brittle fracture accompanied with crack-tip transformation or ductile mechanisms exhibit generally high fracture toughness, which constitute the majority of the outliers seen in Figs. 13(a) and (b). Such tendencies are noticeable for potentials that exhibit high peak stresses and/or highly oscillating TS behaviour, such as EAM-2, EAM-5 or EAM-6. But also the fracture toughness associated with some of the perfectly brittle fractures deviate significantly from the theoretical predictions within the Griffith model. This is related to the significant lattice and bond trapping produced by those potentials, see Table 3.

To investigate these tendencies closer, in Fig. 13(c) and (d) we have compiled maps of the fracture mechanisms against the analytical T_{pl} (see Eq. (11)) and the peak stresses associated with the (110) single-crystal and $\Sigma 5, (310)[001]$ GB decohesion, respectively, which are deemed representative. These maps reveal that plastic mechanisms occur even for cases when $T_{pl} > 1.0$, and the threshold above which only brittle failure occurs increases with increasing peak stress. These findings indicate that the resistance to brittle fracture from the cohesive strength plays an important role when predicting whether brittle or ductile behaviour will ensue.

Because ΔK appears to be higher for potentials whose TS curves are high and narrow, we study how the normalized lattice and bond trapping, $\Delta K / K_{IG}$, vary with the ratio $\sigma_{coh}/\delta_{sep,max}$ for the brittle instances of the (001)[1$\bar{1}$0], (01$\bar{1}$)[$\bar{1}$00] and (110)[$\bar{1}$10] single-crystal systems

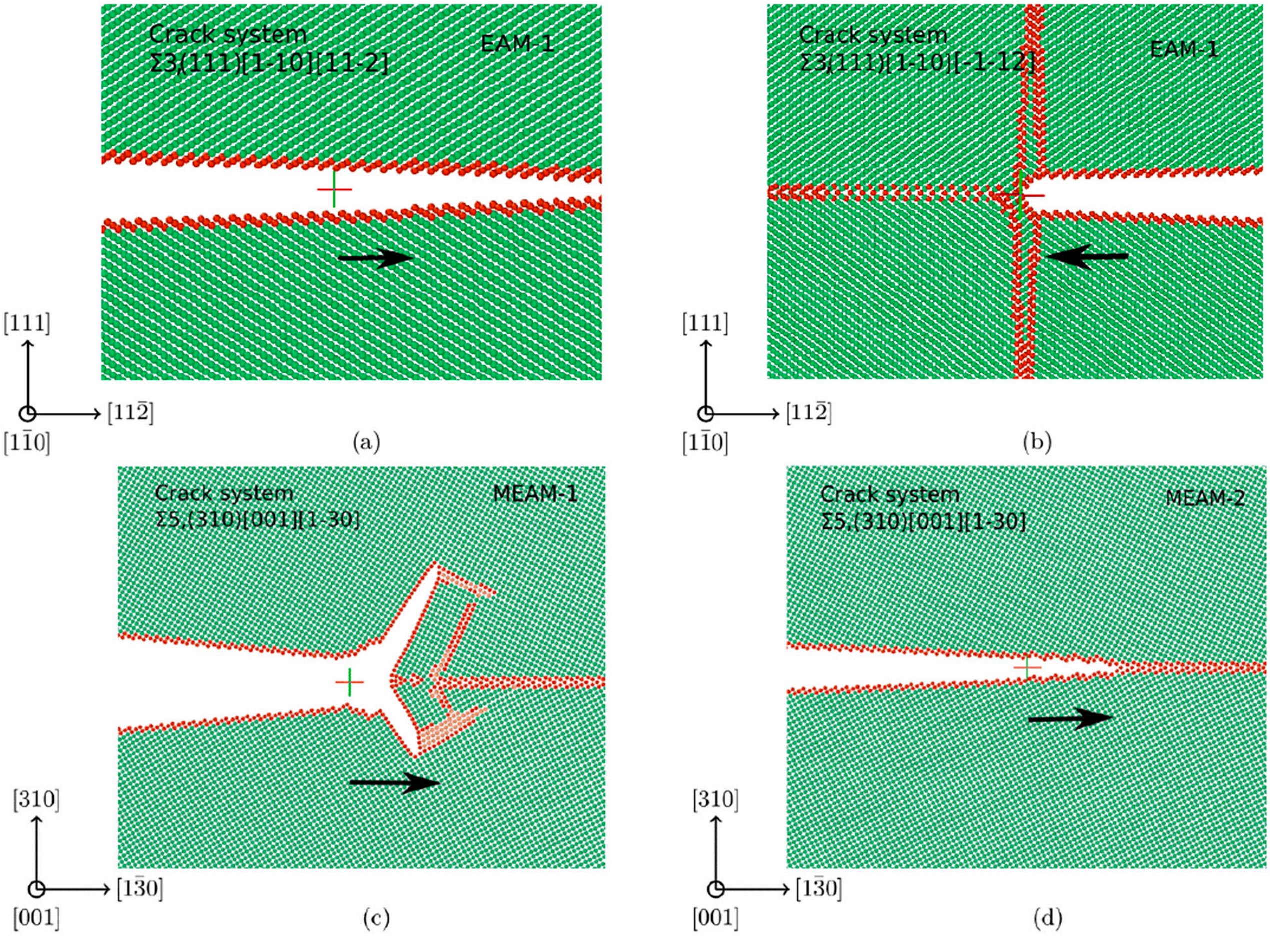

Fig. 12. Influence of the crack propagation direction in $\Sigma3,(111)[1\bar{1}0]$ GB using EAM-1. (a) Brittle growth for propagation direction $[11\bar{2}]$ and (b) twin formation for propagation direction $[\bar{1}\bar{1}2]$. (c) A double-branching and crack-tip transformation, and (d) brittle growth of a crack in $\Sigma5,(310)[001]$ GB with $[1\bar{3}0]$ propagation direction. The particle colouring corresponds to that in Fig. 10. '+' indicates the origin (0,0), which is the initial crack-tip position, and the arrows indicate the crack propagation direction.

along with the $\Sigma3,(111)[1\bar{1}0][1\bar{1}2]$ and $\Sigma9,(114)[1\bar{1}0][22\bar{1}]$ GB systems, see Fig. 13(e) and (f), respectively. Although the lattice/bond trapping varies for different crack systems, it generally increases with increasing $\sigma_{coh}/\delta_{sep,max}$. This is an indication that the post-peak derivative of the TS curves impacts the lattice and bond trapping. Most notably, a rapidly decaying TS curve suggests increased trapping, whereas a slowly decreasing TS curve promotes less. These findings are consistent with the results by Gumbsch and Cannon [92] and the postulation of Sinclair [131] that short interaction range of the interatomic forces yields more significant lattice/bond trapping.

Therefore, an increase in ΔK (or $\Delta K/K_{IG}$) and decrease in T_{pl} implies increased affinity for crack-tip plasticity. Conversely, brittle cleavage is promoted when ΔK and T_{pl} decrease and increase, respectively. These observations appear valid for all systems studied herein and suggest that instead of studying lattice or bond trapping by means of DFT, which is computationally very expensive, the TS-curve can provide an estimate for the magnitude of lattice trapping. Moreover, this implies that interatomic potentials whose TS curves resemble those from DFT should be preferentially used in atomistic studies of fracture.

Although the introduction of GBs generally reduce the critical energy release rate for GB fracture compared to single-crystal fracture (see Eq. (5)), high bond trapping can in principle compensate for the reduction, such that the net fracture toughness increases beyond that of the single-crystal. The only herein observed instances when a crack in a GB was found to withstand a higher stress intensity factor than its single-crystal counterpart was when the brittle failure was accompanied by crack-tip transformation and crack-tip plasticity was seen in corresponding single-crystal. This was seen for instance when EAM-6 was used for a $(112)[1\bar{1}0]$ single-crystal rack and a crack in the $\Sigma3,(112)[1\bar{1}0]$ GB with propagation direction $[\bar{1}\bar{1}1]$. But Möller and Bitzek [33] showed in their simulations with EAM-1 that the maximal bond trapping for certain GB cracks could actually lead to a higher fracture toughness than for single-crystal cracks with the same plane and propagation direction. Although the GB cracks that showed this behaviour were not studied in the present work, we note that the GB cracks in Table 4 experience – even with the MEAM-2 potential – generally higher or comparable bond trapping than lattice trapping in the single-crystal. When using MEAM-2, in particular the $\Sigma5$ and $\Sigma17b$ GBs show toughness values that are in the same range that the toughness for cleavage on the primary planes in single-crystals. This clearly shows that the energy release rate, G_I^{GB}, which according to DFT [62] predicts the $\Sigma3,(112)[1\bar{1}0]$ to be the strongest GB, is insufficient to quantitatively estimate the GB fracture toughness. Interestingly, we also note that the $\Sigma17b,(2\bar{2}3)[110]$ GB, which showed the highest fracture toughness and bond trapping with the MEAM-2 potential (see Table 4), was also reported to show a fairly high fracture strength in Mo [81]. These observations support the notion that some GBs might locally be tougher than single-crystals [33].

6.2. Analytical theories vs. atomistic simulations

For any particular event such as dislocation emission, twin formation or brittle fracture to ensue, the corresponding stress intensity factor must have the lowest value among K_{IE}, K_{IT} and K_{IG}. From Fig. 13, it can be concluded that the numerically measured K_I^{crit} for most cases

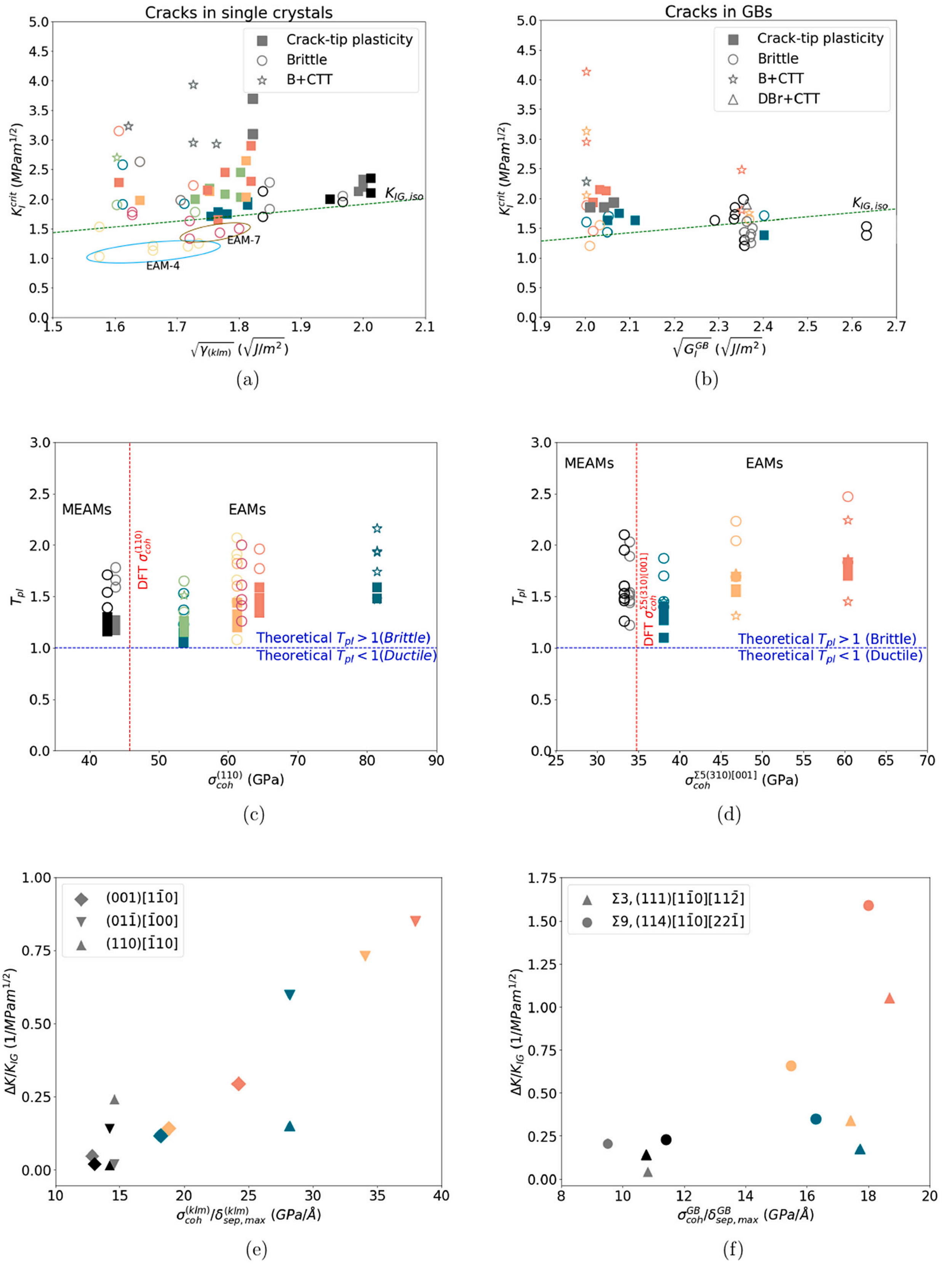

Fig. 13. Resulting K_I^{crit} as function of (a) the surface energy for single-crystals and (b) ideal energy release rate for GBs. The dashed line represents the analytical fracture toughness as computed using Eq. (1). Tendency for plastic deformation as function of (c) $\sigma_{coh}^{(110)}$ in single-crystals and (d) $\sigma_{coh}^{\Sigma5,(310)[001]}$ in GBs. Normalized lattice and bond trapping against the ratio (e) $\sigma_{coh}^{(klm)}/\delta_{sep,max}^{(klm)}$ for single-crystals and (f) $\sigma_{coh}^{GB}/\delta_{sep,max}^{GB}$ GBs. The colouring of markers is the same as in Fig. 4.

Table 5

Performance of potentials in reproducing fracture related properties in comparison with corresponding DFT data. Here, "++", "+" and "−" refer to "consistent" (<10% deviation), "partially consistent" (<20% deviation) and "inconsistent" (>20% deviation) behaviour, respectively. Also, "TS-B" and "mag" are short for smooth, positively skewed bell-shaped TS-behaviour and magnitude, respectively. Finally, "consistent with fracture experiments" refers to consistency of observed mechanisms with experiments.

Potential	Bulk properties			Single-crystal fracture				Bicrystal fracture		
	C_{ij}	$\gamma_{us,(110)}$	γ_{ut}	$\gamma_{(klm)}$-mag	$\sigma_{coh}^{(klm)}$	TS-B$_{(klm)}$	Consistent with fracture experiments	$\sigma_{coh,(GB)}$	TS-B$_{GB}$	γ_{GB}
EAM-1	++	−	−	+	+	++	++	+	+	+
EAM-2	++	+	+	+	−	−	+	−	−	−
EAM-3	++	−	−	−	−	−	+	−	+	+
EAM-4	++	++	++	−	−	−	++	−	−	+
EAM-5	++	+	+	−	−	++	−	−	++	+
EAM-6	++	++	++	−	−	++	−	−	+	++
EAM-7	++	++	++	+	−	−	++	−	−	−
MEAM-1	++	++	+	+	++	++	++	+	++	++
MEAM-2	++	++	++	++	++	++	++	+	++	++

is higher than the analytical K_{IG} in case of brittle fracture, and lower than the analytical K_{IE} and K_{IT} in case of ductile fracture (see Tables S4 and S5, in the supplementary material). Based on our results we can identify a transition interval of $1.0 < T_{pl} \lesssim 1.8$, in which both brittle and ductile mechanisms are observed, see Fig. 13(c) and (d). This suggests that the upper limit of T_{pl} associated with plasticity in practice exceeds the analytical limit of 1.0, see Eq. (11).

There is a number of underlying simplifications associated with the theoretical models that jointly can contribute to the emergence of such variations. For instance, Griffith's theory ignores the influence of the lattice trapping on fracture toughness, which leads to underestimated K_{IG}. Moreover, for a loaded crack-tip, the tensile stress perpendicular to the slip plane reduces the energy barrier for slip at the crack-tip [132], which indicates that there is an interplay between shear and tension. Such normal stress dependence of γ_{us} and γ_{ut} is overlooked by Rice's theory [21], thereby overestimating K_{IE} and K_{IT}. Also, it does not fully account for the local atomic resolution as it does not account for the formation of steps at the crack-tip. Recently, an extended model for crack-tip plasticity was proposed by Andric and Curtin [133], which accounts for such local crack-tip mechanisms. Although this approach was validated only for FCC materials, it seems to yield predictions that are in better agreement with atomistic simulations.

6.3. Applicability of potentials for fracture modelling

To be useful in fracture simulations, potentials first and foremost have to be free of unphysical artefacts like oscillating TS curves or phase transformations. From this perspective, only EAM-1, EAM-5 and EAM-6 along with MEAM-1 and MEAM-2 show TS curves that are free of artefacts.

It is further necessary to reproduce the relevant material properties well, and to be consistent with the experimentally observed low-temperature fracture behaviour. In Table 5 we have summarized the performance of the potentials. The elastic properties are well-represented by all potentials. The energies of low-index surfaces are, however, generally too low for the EAM potentials, while they are reproduced well by MEAM-1 and MEAM-2 compared to DFT, see Fig. 3. Further differences exist with respect to the unstable stacking fault and unstable twinning fault energies.

The comparison of the qualitative fracture behaviour found in simulations with the experimental findings is not straightforward. The simulation setup with short periodic crack fronts precludes crack propagation on oblique planes, as would be necessary to explain the observation of faceted crack surfaces [38,46], like the ones observed experimentally for the $\{111\}\langle 011\rangle$ cracks [46]. Similarly, the setup does not allow for the formation of a faceted crack front that would allow the crack to propagate along easy directions [38,51].

We note that the ductile behaviour observed in simulations with EAM-5 and EAM-6 for $\{110\}\langle\bar{1}10\rangle$ cracks deviates from experimental observations, since no traces crack-tip blunting by dislocations were observed in experiments. Instead, the behaviour of the EAM-1, MEAM-1 and MEAM-2 potentials, which consistently show brittle fracture for cracks on the primary and secondary cleavage planes, is more in line with experimental observations. However, these potentials predict a deflection of $\{001\}\langle 0\bar{1}0\rangle$ cracks onto $\{101\}$ planes, which is not observed experimentally. But this discrepancy could be explained by the crack front on $\{001\}$ having the ability to locally propagate along two easy $\langle 110\rangle$ directions that are inclined 45° to the main crack propagation direction [51], which is not practically possible to reproduce in the simulations due to the limited spatial extension in the periodic direction, see Fig. 2.

Moreover, EAM-1, MEAM-1 and MEAM-2 also show the lowest fracture toughness value for the $\{110\}\langle\bar{1}10\rangle$ crack and not the $\{01\bar{1}\}\langle\bar{1}00\rangle$ crack. This is in accordance with experimental measurements, although we note that the experimental values of the fracture toughness for both of these crack systems lie within the error margins of each other [38], see Table 3.

None of the potentials reproduced the experimentally observed deviation of the $\{112\}$ crack plane onto the $\{100\}$ plane for $\{112\}\langle\bar{1}10\rangle$ cracks [46]. For this crack system, the potentials with comparatively low γ_{ut} compared with DFT showed twinning, see Fig. 5, while the remaining potentials showed brittle fracture on the original crack plane.

Unlike EAM-1, both MEAM-1 and MEAM-2 lead to γ_{GB} values in agreement with DFT [62] and match the TS curves for both single- and bicrystals. But MEAM-1 more severely underestimates γ_{ut} and overestimates $\gamma_{(112)}$ compared with DFT, and it further showed unexpected crack branching for one of the GBs. Based on these observations and the overall comparison in Table 5, MEAM-2 currently seems to be the best suited potential for simulating cleavage fracture in single- and polycrystalline tungsten. The MEAM potentials, however, require one order of magnitude more computing time than the EAM potentials, see Table S2 in the supplementary material. Among the EAM potentials, only EAM-1 can be regarded acceptable for fracture studies, although it is noted that it exhibits a lattice trapping range that is one order of magnitude larger than what would be expected from the DFT TS curves and the MEAM potentials.

7. Summary and conclusions

Among the considered potentials, it is concluded that the new MEAM-2 potential developed here is the most suitable for fracture simulations. Not only does it reproduce the TS curve and all fracture-relevant DFT data well, it showed no crack-tip artefacts for any of the studied systems and it behaves consistently with fracture experiments for cracks on the primary and secondary cleavage planes. It is thus expected to constitute an important tool for future atomistic studies of fracture in tungsten.

Several of the EAM potentials, showed strong artefacts such as artificial crack-tip transformation, negative traction and violent oscillatory behaviour in the TS curves. Furthermore, large variations in surface and GB energy were observed. Of the EAM potentials, only EAM-1 performed reasonably well. It does, however, underestimate the unstable stacking fault energy and exhibit up to one order of magnitude higher lattice/bond trapping than the MEAM potentials.

We find that high lattice/bond trapping is characteristic for all studied EAM potentials, and it correlates directly to the interaction range and peak stress of the TS curve. Our general observation is that potentials with short interaction range and high peak stress yield high lattice trapping. This has important consequences for the fracture behaviour: Large lattice trapping significantly increases the critical stress intensity factor associated with brittle cleavage, K_{IG}, sometimes to the extent that alternative crack-tip processes – such as emission of dislocations or twins – may occur instead, even if they are associated with higher K-values than K_{IG}. Lattice trapping can thus directly affect the qualitative fracture behaviour. This is of particular importance in GB fracture, as the magnitude of the bond trapping varies with the crack-tip location in the structural unit, and it locally can become very large — such that the fracture toughness significantly exceeds that predicted from Griffith theory.

For all potentials it is found that the Griffith and Rice theories fail to predict the fracture behaviour, as well as the fracture toughness. Instead, quasi-static fracture simulations can be carried out to determine them for any given material and crack orientation. These calculations are currently still too computationally challenging to be carried out routinely with DFT. But comparison of TS curves obtained by empirical potentials with those from DFT calculations has proved to be a quick way of assessing a potential's applicability to fracture simulations.

CRediT authorship contribution statement

Praveenkumar Hiremath: Conceptualization, Methodology - potential refining, Molecular statics, Investigation, Analysis, Writing – original draft. **Solveig Melin:** Writing – review & editing. **Erik Bitzek:** Conceptualization, Analysis, Writing – review & editing. **Pär A.T. Olsson:** Conceptualization, Methodology - density functional theory, Analysis, Potential fitting, Writing – review & editing.

Declaration of competing interest

The authors declare that they have no known competing financial interests or personal relationships that could have appeared to influence the work reported in this paper.

Data availability statement

The data required to reproduce these findings will be provided by the corresponding author upon reasonable request. The MEAM-2 potential files for LAMMPS are available as part of the supplementary material at https://doi.org/10.1016/j.commatsci.2022.111283.

Acknowledgements

PH and PATO gratefully acknowledge funding from the Swedish Research Council (grant agreement No 2016-04162). EB gratefully acknowledges funding from the European Research Council (ERC) under the European Union's Horizon 2020 research and innovation programme (grant agreement No 725483). The computations were enabled by resources provided by the Swedish National Infrastructure for Computing (SNIC) at the National Supercomputer Centre (NSC), Linköping University, and at the High Performance Computing Centre North (HPC2N), Umeå University, partially funded by the Swedish Research Council through grant agreement No 2018-05973.

Appendix A. Supplementary data

Supplementary material related to this article can be found online at https://doi.org/10.1016/j.commatsci.2022.111283.

References

[1] S.J. Zinkle, Fusion materials science: Overview of challenges and recent progress, Phys. Plasmas 12 (5) (2005) 058101.

[2] S. Matsuda, K. Tobita, Evolution of the ITER program and prospect for the next-step fusion DEMO reactors: status of the fusion energy R&D as ultimate source of energy, J. Nucl. Sci. Technol. 50 (4) (2013) 321–345.

[3] G. Federici, A. Zhitlukhin, N. Arkhipov, R. Giniyatulin, N. Klimov, I. Landman, V. Podkovyrov, V. Safronov, A. Loarte, M. Merola, Effects of ELMs and disruptions on ITER divertor armour materials, J. Nucl. Mater. 337–339 (2005) 684–690.

[4] J. Pamela, A. Bécoulet, D. Borba, J.L. Boutard, L. Horton, D. Maisonnier, Efficiency and availability driven R&D issues for DEMO, Fusion Eng. Des. 84 (2–6) (2009) 194–204.

[5] P.A.T. Olsson, J. Blomqvist, Intergranular fracture of tungsten containing phosphorus impurities: A first principles investigation, Comput. Mater. Sci. 139 (2017) 368–378.

[6] M. Rieth, J.L. Boutard, S.L. Dudarev, T. Ahlgren, S. Antusch, N. Baluc, M.F. Barthe, C.S. Becquart, L. Ciupinski, J.B. Correia, et al., Review on the EFDA programme on tungsten materials technology and science, J. Nucl. Mater. 417 (1–3) (2011) 463–467.

[7] M. Rieth, S.L. Dudarev, S.G. De Vicente, J. Aktaa, T. Ahlgren, S. Antusch, D.E.J. Armstrong, M. Balden, N. Baluc, M.F. Barthe, et al., A brief summary of the progress on the EFDA tungsten materials program, J. Nucl. Mater. 442 (1–3) (2013) S173–S180.

[8] H. Bolt, V. Barabash, G. Federici, J. Linke, A. Loarte, J. Roth, K. Sato, Plasma facing and high heat flux materials–needs for ITER and beyond, J. Nucl. Mater. 307 (2002) 43–52.

[9] P. Norajitra, S.I. Abdel-Khalik, L.M. Giancarli, T. Ihli, G. Janeschitz, S. Malang, I.V. Mazul, P. Sardain, Divertor conceptual designs for a fusion power plant, Fusion Eng. Des. 83 (7–9) (2008) 893–902.

[10] D. Maisonnier, D. Campbell, I. Cook, L. Di Pace, L. Giancarli, J. Hayward, A.L. Puma, M. Medrano, P. Norajitra, M. Roccella, et al., Power plant conceptual studies in Europe, Nucl. Fusion 47 (11) (2007) 1524.

[11] P. Gumbsch, J. Riedle, A. Hartmaier, H.F. Fischmeister, Controlling factors for the brittle-to-ductile transition in tungsten single crystals, Science 282 (5392) (1998) 1293–1295.

[12] A. Giannattasio, S.G. Roberts, Strain-rate dependence of the brittle-to-ductile transition temperature in tungsten, Phil. Mag. 87 (17) (2007) 2589–2598.

[13] E. Gaganidze, D. Rupp, J. Aktaa, Fracture behaviour of polycrystalline tungsten, J. Nucl. Mater. 446 (1–3) (2014) 240–245.

[14] M. Wirtz, I. Uytdenhouwen, V. Barabash, F. Escourbiac, T. Hirai, J. Linke, T. Loewenhoff, S. Panayotis, G. Pintsuk, Material properties and their influence on the behaviour of tungsten as plasma facing material, Nucl. Fusion 57 (6) (2017) 066018.

[15] A. Giannattasio, Z. Yao, E. Tarleton, S. Roberts, Brittle–ductile transitions in polycrystalline tungsten, Phil. Mag. 90 (30) (2010) 3947–3959.

[16] V. Philipps, Tungsten as material for plasma-facing components in fusion devices, J. Nucl. Mater. 415 (1) (2011) S2–S9.

[17] L. Gharaee, First Principles Study of Tungsten-Based Alloys: From Defect Thermodynamics to Phase Diagrams (Ph.D. thesis), Department of Chemistry and Chemical Engineering, Chalmers University of Technology, 2017.

[18] Y. Zhang, A.V. Ganeev, J.T. Wang, J.Q. Liu, I.V. Alexandrov, Observations on the ductile-to-brittle transition in ultrafine-grained tungsten of commercial purity, Mater. Sci. Eng. A 503 (1–2) (2009) 37–40.

[19] B.G. Butler, J.D. Paramore, J.P. Ligda, C. Ren, Z.Z. Fang, S.C. Middlemas, K.J. Hemker, Mechanisms of deformation and ductility in tungsten – A review, Int. J. Refract. Met. Hard Mater. 75 (2018) 248–261.

[20] P. Gumbsch, Modelling brittle and semi-brittle fracture processes, Mater. Sci. Eng. A 319 (2001) 1–7.

[21] J.R. Rice, Dislocation nucleation from a crack tip: an analysis based on the Peierls concept, J. Mech. Phys. Solids 40 (2) (1992) 239–271.

[22] G. Schoeck, W. Pichl, Bond trapping of cracks, Phys. Status Solidi A 118 (1) (1990) 109–115.

[23] E. Bitzek, J.R. Kermode, P. Gumbsch, Atomistic aspects of fracture, Int. J. Fract. 191 (1–2) (2015) 13–30.

[24] M.S. Daw, M.I. Baskes, Embedded-atom method: Derivation and application to impurities, surfaces, and other defects in metals, Phys. Rev. B 29 (12) (1984) 6443.

[25] M.S. Daw, M.I. Baskes, Semiempirical, quantum mechanical calculation of hydrogen embrittlement in metals, Phys. Rev. Lett. 50 (17) (1983) 1285.

[26] M.S. Daw, S.M. Foiles, M.I. Baskes, The embedded-atom method: a review of theory and applications, Mater. Sci. Rep. 9 (1993) 251–310.

[27] M.I. Baskes, Modified embedded-atom potentials for cubic materials and impurities, Phys. Rev. B 46 (5) (1992) 2727.

[28] M.C. Marinica, L. Ventelon, M. Gilbert, L. Proville, S. Dudarev, J. Marian, G. Bencteux, F. Willaime, Interatomic potentials for modelling radiation defects and dislocations in tungsten, J. Phys.: Condens. Matter 25 (39) (2013) 395502.

[29] V.L. Deringer, M.A. Caro, G. Csányi, Machine learning interatomic potentials as emerging tools for materials science, Adv. Mater. 31 (46) (2019) 1902765.

[30] S. Starikov, D. Smirnova, T. Pradhan, Y. Lysogorskiy, H. Chapman, M. Mrovec, R. Drautz, Angular-dependent interatomic potential for large-scale atomistic simulation of iron: Development and comprehensive comparison with existing interatomic models, Phys. Rev. Mater. 5 (2021) 063607.

[31] G. Bonny, A. Bakaev, D. Terentyev, Y.A. Mastrikov, Interatomic potential to study plastic deformation in tungsten-rhenium alloys, J. Appl. Phys. 121 (16) (2017) 165107.

[32] L.X. Liu, X.C. Li, Y.C. Chen, W.Y. Hu, G.N. Luo, F. Gao, H.Q. Deng, Evaluation of tungsten interatomic potentials for radiation damage simulations, Tungsten 2 (1) (2020) 3–14.

[33] J.J. Möller, E. Bitzek, Fracture toughness and bond trapping of grain boundary cracks, Acta Mater. 73 (2014) 1–11.

[34] V.R. Coffman, J.P. Sethna, A. Ingraffea, J. Bozek, N. Bailey, E. Barker, Challenges in continuum modelling of intergranular fracture, Strain 47 (2011) 99–104.

[35] B. Paliwal, M. Cherkaoui, An improved atomistic simulation based mixed-mode cohesive zone law considering non-planar crack growth, Int. J. Solids Struct. 50 (20–21) (2013) 3346–3360.

[36] J. Lloyd, J. Zimmerman, R. Jones, X. Zhou, D. McDowell, Finite element analysis of an atomistically derived cohesive model for brittle fracture, Modelling Simulation Mater. Sci. Eng. 19 (6) (2011) 065007.

[37] A. Needleman, An analysis of tensile decohesion along an interface, J. Mech. Phys. Solids 38 (3) (1990) 289–324.

[38] J. Riedle, P. Gumbsch, H.F. Fischmeister, Cleavage anisotropy in tungsten single crystals, Phys. Rev. Lett. 76 (19) (1996) 3594.

[39] D. Hull, P. Beardmore, A. Valintine, Crack propagation in single crystals of tungsten, Philos. Mag.: J. Theor. Exp. Appl. Phys. 12 (119) (1965) 1021–1041.

[40] J. Cordwell, D. Hull, Observation of {110} cleavage in ⟨110⟩ axis tungsten single crystals, Phil. Mag. 26 (1) (1972) 215–224.

[41] J. Cordwell, D. Hull, Effect of specimen thickness on the fracture surface energy of ⟨100⟩ axis tungsten single crystals, Phil. Mag. 27 (5) (1973) 1183–1192.

[42] J. Cordwell, D. Hull, The brittle fracture of [100] axis tungsten single crystals, Phil. Mag. 19 (161) (1969) 951–966.

[43] J. Liu, J. Bilello, Effects of plastic relaxation on the semi-brittle fracture of ⟨100⟩ oriented tungsten single crystals, Phil. Mag. 35 (6) (1977) 1453–1472.

[44] S. Kalácska, J. Ast, P.D. Ispánovity, J. Michler, X. Maeder, 3D HR-EBSD characterization of the plastic zone around crack tips in tungsten single crystals at the micron scale, Acta Mater. 200 (2020) 211–222.

[45] J. Riedle, P. Gumbsch, H. Fischmeister, V. Glebovsky, V. Semenov, Fracture studies of tungsten single crystals, Mater. Lett. 20 (5–6) (1994) 311–317.

[46] J. Riedle, Bruchwiderstand in Wolfram-Einkristallen: Einfluß der Kristallographischen Orientierung, der Temperatur und der Lastrate, VDI-Verlag, 1995.

[47] C. Bohnert, N. Schmitt, S. Weygand, O. Kraft, R. Schwaiger, Fracture toughness characterization of single-crystalline tungsten using notched micro-cantilever specimens, Int. J. Plast. 81 (2016) 1–17.

[48] J. Ast, M. Göken, K. Durst, Size-dependent fracture toughness of tungsten, Acta Mater. 138 (2017) 198–211.

[49] J. Ast, J. Schwiedrzik, J. Wehrs, D. Frey, M.N. Polyakov, J. Michler, X. Maeder, The brittle-ductile transition of tungsten single crystals at the micro-scale, Mater. Des. 152 (2018) 168–180.

[50] R. Abernethy, J.L. Gibson, A. Giannattasio, J. Murphy, O. Wouters, S. Bradnam, L. Packer, M. Gilbert, M. Klimenkov, M. Rieth, et al., Effects of neutron irradiation on the brittle to ductile transition in single crystal tungsten, J. Nucl. Mater. 527 (2019) 151799.

[51] S. Kohlhoff, P. Gumbsch, H. Fischmeister, Crack propagation in bcc crystals studied with a combined finite-element and atomistic model, Phil. Mag. A 64 (4) (1991) 851–878.

[52] P. Gumbsch, Atomistische Modellierung Zweidimensionaler Defekte in Metallen: Risse, Phasengrenzflächen (Dissertation), Universität Stuttgart, 1991.

[53] Y. Furuya, H. Noguchi, Combined method of molecular dynamics with micromechanics in simulations of crack propagation, Mater. Trans. 42 (1) (2001) 45–51.

[54] W.S. Ko, B.J. Lee, Origin of unrealistic blunting during atomistic fracture simulations based on MEAM potentials, Phil. Mag. 94 (16) (2014) 1745–1753.

[55] X. Yu, F. Gou, B. Li, N. Zhang, Numerical study of the effect of hydrogen on the crack propagation behavior of single crystal tungsten, Fusion Eng. Des. 89 (7–8) (2014) 1096–1100.

[56] X.T. Shu, S.F. Xiao, H.Q. Deng, L. Ma, W. Hu, Atomistic simulation of crack propagation in single crystal tungsten under cyclic loading, J. Mater. Res. 32 (8) (2017) 1474–1483.

[57] J.J. Möller, E. Bitzek, R. Janisch, H. ul Hassan, A. Hartmaier, Fracture ab initio: A force-based scaling law for atomistically informed continuum models, J. Mater. Res. 33 (22) (2018) 3750–3761.

[58] J.J. Möller, Atomistic Simulations on Grain Boundary Fracture in Tungsten Bicrystals (Diploma Thesis), Friedrich - Alexander - Universität Erlangen - Nürnberg, 2011.

[59] A.A. Griffith, The phenomena of rupture and flow in solids, Philos. Trans. R. Soc. Lond. Ser. A 221 (582–593) (1921) 163–198.

[60] D. Roundy, C.R. Krenn, M.L. Cohen, J.W.M. Jr., The ideal strength of tungsten, Phil. Mag. A 81 (7) (2001) 1725–1747.

[61] P. Lazar, R. Podloucky, Cleavage fracture of a crystal: Density functional theory calculations based on a model which includes structural relaxations, Phys. Rev. B 78 (2008) 104114.

[62] D. Scheiber, R. Pippan, P. Puschnig, L. Romaner, Ab initio calculations of grain boundaries in bcc metals, Modelling Simulation Mater. Sci. Eng. 24 (3) (2016) 035013.

[63] L. Borgsmiller, M.T. Agne, J.P. Male, S. Anand, G. Li, S.I. Morozov, G.J. Snyder, Estimating the lower-limit of fracture toughness from ideal-strength calculations, Mater. Horiz. (2022).

[64] J.J. Möller, Atomistic Simulations of Crack Front Curvature Effects and Crack-Microstructure Interactions (Ph.D. thesis), Friedrich - Alexander - Universität Erlangen - Nürnberg, 2017.

[65] L. Banks-Sills, Interface Fracture and Delaminations in Composite Materials, Springer, 2018.

[66] R. Margevicius, J. Riedle, P. Gumbsch, Fracture toughness of polycrystalline tungsten under mode I and mixed mode horizoi/II loading, Mater. Sci. Eng. A 270 (2) (1999) 197–209.

[67] D. Rupp, S.M. Weygand, Experimental investigation of the fracture toughness of polycrystalline tungsten in the brittle and semi-brittle regime, J. Nucl. Mater. 386 (2009) 591–593.

[68] D. Rupp, S.M. Weygand, Loading rate dependence of the fracture toughness of polycrystalline tungsten, J. Nucl. Mater. 417 (1–3) (2011) 477–480.

[69] D. Rupp, S. Weygand, Anisotropic fracture behaviour and brittle-to-ductile transition of polycrystalline tungsten, Phil. Mag. 90 (30) (2010) 4055–4069.

[70] B. Gludovatz, S. Wurster, A. Hoffmann, R. Pippan, A study into the crack propagation resistance of pure tungsten, Eng. Fract. Mech. 100 (2013) 76–85.

[71] V. Nikolić, S. Wurster, D. Firneis, R. Pippan, Fracture toughness evaluation of UFG tungsten foil, Int. J. Refract. Met. Hard Mater. 76 (2018) 214–225.

[72] D. Rupp, R. Mönig, P. Gruber, S. Weygand, Fracture toughness and microstructural characterization of polycrystalline rolled tungsten, Int. J. Refract. Met. Hard Mater. 28 (6) (2010) 669–673.

[73] C. Yin, D. Terentyev, T. Pardoen, R. Petrov, Z. Tong, Ductile to brittle transition in ITER specification tungsten assessed by combined fracture toughness and bending tests analysis, Mater. Sci. Eng. A 750 (2019) 20–30.

[74] O. Dudka, V. Ksenofontov, E. Sadanov, I. Starchenko, T. Mazilova, I. Mikhailovskij, Special grain boundaries in ultrafine-grained tungsten, Nanoscale Res. Lett. 11 (1) (2016) 1–7.

[75] B. Gludovatz, S. Wurster, T. Weingärtner, A. Hoffmann, R. Pippan, Influence of impurities on the fracture behaviour of tungsten, Phil. Mag. 91 (22) (2011) 3006–3020.

[76] C. Bonnekoh, J. Reiser, A. Hartmaier, S. Bonk, A. Hoffmann, M. Rieth, The brittle-to-ductile transition in cold-rolled tungsten sheets: the rate-limiting mechanism of plasticity controlling the BDT in ultrafine-grained tungsten, J. Mater. Sci. 55 (2020) 12314–12337.

[77] J.M. Liu, B.-W. Shen, Grain boundary fracture in tungsten bi-crystals, Acta Metall. 30 (6) (1982) 1197–1202.

[78] A.P. Sutton, R.W. Balluffi, Interfaces in Crystalline Materials, Clarendon, Oxford, 1995.

[79] J.M. Liu, B. Shen, Direct measurement of the work of fracture for grain boundaries of twist misorientation about ⟨100⟩ in tungsten, Metall. Mater. Trans. A 15 (6) (1984) 1289–1292.

[80] H. Kurishita, A. Ôishi, H. Kubo, H. Yoshinaga, Grain boundary fracture in molybdenum bicrystals with various ⟨110⟩ symmetric tilt boundaries, Trans. Jpn. Inst. Met. 26 (5) (1985) 341–352.

[81] S. Tsurekawa, T. Tanaka, H. Yoshinaga, Grain boundary structure, energy and strength in molybdenum, Mater. Sci. Eng. A 176 (1–2) (1994) 341–348.

[82] I. Mikhailovskij, T. Mazilova, V. Voyevodin, A. Mazilov, Inherent strength of grain boundaries in tungsten, Phys. Rev. B 83 (13) (2011) 134115.

[83] E. Sadanov, T. Mazilova, V. Ksenofontov, I. Starchenko, I. Mikhailovskij, Special non-CSL grain boundaries in tungsten: misorientation distribution and energetics, Mater. Lett. 145 (2015) 137–140.

[84] H. Zheng, X.-G. Li, R. Tran, C. Chen, M. Horton, D. Winston, K.A. Persson, S.P. Ong, Grain boundary properties of elemental metals, Acta Mater. 186 (2020) 40–49.

[85] A.A. Griffith, VI. The phenomena of rupture and flow in solids, Philos. Trans. R. Soc. A 221 (582–593) (1921) 163–198.

[86] J.R. Rice, Mathematical analysis in the mechanics of fracture, in: H. Liebowitz (Ed.), Fracture: An Advanced Treatise, in: Mathematical Fundamentals, vol. 2, Academic Press, NY, 1968, pp. 191–311, Ch. 3.

[87] G.C. Sih, H. Liebowitz, Mathematical theories of brittle fracture, in: H. Liebowitz (Ed.), Fracture: An Advanced Treatise, in: Mathematical Fundamentals, vol. 2, Academic Press, NY, 1968, pp. 67–190, Ch. 2.

[88] G.C. Sih, P. Paris, G. Irwin, On cracks in rectilinearly anisotropic bodies, Int. J. Fract. Mech. 1 (3) (1965) 189–203.

[89] D. Lieberman, S. Zirinsky, A simplified calculation for the elatic constants of arbitrarily oriented single crystals, Acta Crystallogr. 9 (5) (1956) 431–436.

[90] M. Lane, Interface fracture, Annu. Rev. Mater. Res. 33 (1) (2003) 29–54.

[91] R. Thomson, C. Hsieh, V. Rana, Lattice trapping of fracture cracks, J. Appl. Phys. 42 (8) (1971) 3154–3160.

[92] P. Gumbsch, R.M. Cannon, Atomistic aspects of brittle fracture, MRS Bull. 25 (5) (2000) 15–20.

[93] M. Marder, Effects of atoms on brittle fracture, Int. J. Fract. 130 (2) (2004) 517–555.

[94] D. Farkas, Fracture mechanisms of symmetrical tilt grain boundaries, Phil. Mag. Lett. 80 (4) (2000) 229–237.

[95] E. Tadmor, N. Bernstein, A first-principles measure for the twinnability of FCC metals, J. Mech. Phys. Solids 52 (11) (2004) 2507–2519.

[96] E. Tadmor, S. Hai, A Peierls criterion for the onset of deformation twinning at a crack tip, J. Mech. Phys. Solids 51 (5) (2003) 765–793.

[97] M.W. Finnis, J.E. Sinclair, A simple empirical N-body potential for transition metals, Phil. Mag. A 50 (1) (1984) 45–55.

[98] G. Ackland, R. Thetford, An improved N-body semi-empirical model for body-centred cubic transition metals, Phil. Mag. A 56 (1) (1987) 15–30.

[99] S. Han, L.A. Zepeda-Ruiz, G.J. Ackland, R. Car, D.J. Srolovitz, Interatomic potential for vanadium suitable for radiation damage simulations, J. Appl. Phys. 93 (6) (2003) 3328–3335.

[100] J. Wang, Y. Zhou, M. Li, Q. Hou, A modified W–W interatomic potential based on ab initio calculations, Modelling Simulation Mater. Sci. Eng. 22 (1) (2013) 015004.

[101] P.A.T. Olsson, Semi-empirical atomistic study of point defect properties in BCC transition metals, Comput. Mater. Sci. 47 (1) (2009) 135–145.

[102] X. Zhou, R. Johnson, H. Wadley, Misfit-energy-increasing dislocations in vapor-deposited CoFe/NiFe multilayers, Phys. Rev. B 69 (14) (2004) 144113.

[103] B.-J. Lee, M. Baskes, H. Kim, Y.K. Cho, Second nearest-neighbor modified embedded atom method potentials for bcc transition metals, Phys. Rev. B 64 (18) (2001) 184102.

[104] J. Möller, E. Bitzek, Atomic-scale modeling of elementary processes during the fatigue of metallic materials: from crack initiation to crack-microstructure interactions, in: H.J. Christ (Ed.), Fatigue of Materials at Very High Numbers of Loading Cycles, Springer, 2018, pp. 25–48, Ch. 2.

[105] S. Plimpton, Fast parallel algorithms for short-range molecular dynamics, J. Comput. Phys. 117 (1) (1995) 1–19.

[106] A.P. Thompson, H.M. Aktulga, R. Berger, D.S. Bolintineanu, W.M. Brown, P.S. Crozier, P.J. in 't Veld, A. Kohlmeyer, S.G. Moore, T.D. Nguyen, R. Shan, M.J. Stevens, J. Tranchida, C. Trott, S.J. Plimpton, LAMMPS - a flexible simulation tool for particle-based materials modeling at the atomic, meso, and continuum scales, Comput. Phys. Comm. 271 (2022) 108171.

[107] J.P. Perdew, K. Burke, M. Ernzerhof, Generalized gradient approximation made simple, Phys. Rev. Lett. 77 (1996) 3865–3868.

[108] J.P. Perdew, K. Burke, M. Ernzerhof, Generalized gradient approximation made simple [erratum], Phys. Rev. Lett. 78 (1997) 1396.

[109] G. Kresse, J. Hafner, *Ab initio* molecular dynamics for liquid metals, Phys. Rev. B 47 (1993) 558–561.

[110] G. Kresse, J. Hafner, *Ab initio* molecular-dynamics simulation of the liquid-metal amorphous-semiconductor transition in germanium, Phys. Rev. B 49 (1994) 14251–14269.

[111] G. Kresse, J. Furthmüller, Efficient iterative schemes for *ab initio* total-energy calculations using a plane-wave basis set, Phys. Rev. B 54 (1996) 11169–11186.

[112] G. Kresse, J. Furthmüller, Efficiency of ab-initio total energy calculations for metals and semiconductors using a plane-wave basis set, Comput. Mater. Sci. 6 (1) (1996) 15–50.

[113] A.H. Faisal, C.R. Weinberger, Modeling twin boundary structures in body centered cubic transition metals, Comput. Mater. Sci. 197 (2021) 110649.

[114] A. Ojha, H. Sehitoglu, Twinning stress prediction in bcc metals and alloys, Phil. Mag. Lett. 94 (10) (2014) 647–657.

[115] O. Nguyen, M. Ortiz, Coarse-graining and renormalization of atomistic binding relations and universal macroscopic cohesive behavior, J. Mech. Phys. Solids 50 (8) (2002) 1727–1741.

[116] M. Wojdyr, S. Khalil, Y. Liu, I. Szlufarska, Energetics and structure of $\langle 001 \rangle$ tilt grain boundaries in SiC, Modelling Simulation Mater. Sci. Eng. 18 (7) (2010) 075009.

[117] K.S. Cheung, S. Yip, A molecular-dynamics simulation of crack-tip extension: the brittle-to-ductile transition, Modelling Simulation Mater. Sci. Eng. 2 (4) (1994) 865.

[118] R.C. Ehemann, J.W. Nicklas, H. Park, J.W. Wilkins, Ab initio based empirical potential applied to tungsten at high pressure, Phys. Rev. B 95 (18) (2017) 184101.

[119] L. Vitos, A. Ruban, H.L. Skriver, J. Kollar, The surface energy of metals, Surf. Sci. 411 (1–2) (1998) 186–202.

[120] F.E. Neumann, O.E. Meyer, Vorlesungen über die Theorie der Elasticität der Festen Körper und des Lichtäthers, Gehalten an der Universität Königsberg, McGraw-Hill, 1885, http://hdl.handle.net/2027/uc1.$b530647.

[121] V. Vitek, Intrinsic stacking faults in body-centred cubic crystals, Phil. Mag. 18 (154) (1968) 773–786.

[122] J.J. Möller, M. Mrovec, I. Bleskov, J. Neugebauer, T. Hammerschmidt, R. Drautz, C. Elsässer, T. Hickel, E. Bitzek, $\{110\}$ Planar faults in strained bcc metals: Origins and implications of a commonly observed artifact of classical potentials, Phys. Rev. Mater. 2 (9) (2018) 093606.

[123] S. Xu, J.K. Startt, T.G. Payne, C.S. Deo, D.L. McDowell, Size-dependent plastic deformation of twinned nanopillars in body-centered cubic tungsten, J. Appl. Phys. 121 (17) (2017) 175101.

[124] D. Faken, H. Jonsson, Systematic analysis of local atomic structure combined with 3D computer graphics, Comput. Mater. Sci. 2 (2) (1994) 279–286.

[125] P. Gumbsch, Brittle fracture and the brittle-to-ductile transition of tungsten, J. Nucl. Mater. 323 (2–3) (2003) 304–312.

[126] J.J. Möller, E. Bitzek, Comparative study of embedded atom potentials for atomistic simulations of fracture in α-iron, Modelling Simulation Mater. Sci. Eng. 22 (4) (2014) 045002.

[127] J.-S. Wang, P. Anderson, Fracture behavior of embrittled F.C.C. metal bicrystals, Acta Metall. Mater. 39 (5) (1991) 779–792.

[128] F. Cleri, S.R. Phillpot, D. Wolf, Atomistic simulations of integranular fracture in symmetric-tilt grain boundaries, Interface Sci. 7 (1) (1999) 45–55.

[129] A. Argon, S. Maloof, Plastic deformation of tungsten single crystals at low temperatures, Acta Metall. 14 (11) (1966) 1449–1462.

[130] J.W. Christian, Some surprising features of the plastic deformation of body-centered cubic metals and alloys, Metall. Trans. A 14 (7) (1983) 1237–1256.

[131] J.E. Sinclair, The influence of the interatomic force law and of kinks on the propagation of brittle cracks, Philos. Mag.: J. Theor. Exp. Appl. Phys. 31 (3) (1975) 647–671.

[132] Y. Sun, G.E. Beltz, J.R. Rice, Estimates from atomic models of tension-shear coupling in dislocation nucleation from a crack tip, Mater. Sci. Eng. A 170 (1–2) (1993) 67–85.

[133] P. Andric, W. Curtin, New theory for Mode I crack-tip dislocation emission, J. Mech. Phys. Solids 106 (2017) 315–337.